

# Instability of Supersonic Cold Streams Feeding Galaxies IV: Survival of Radiatively Cooling Streams

Nir Mandelker<sup>1,2\*</sup>, Daisuke Nagai<sup>1,3</sup>, Han Aung<sup>3</sup>, Avishai Dekel<sup>4</sup>, Yuval Birnboim<sup>4</sup>,  
Frank C. van den Bosch<sup>1</sup>

<sup>1</sup>*Department of Astronomy, Yale University, PO Box 208101, New Haven, CT, USA;*

<sup>2</sup>*Heidelberger Institut für Theoretische Studien, Schloss-Wolfsbrunnengasse 35, 69118 Heidelberg, Germany;*

<sup>3</sup>*Department of Physics, Yale University, New Haven, CT 06520, USA;*

<sup>4</sup>*Centre for Astrophysics and Planetary Science, Racah Institute of Physics, The Hebrew University, Jerusalem 91904, Israel*

## ABSTRACT

We study the effects of Kelvin Helmholtz Instability (KHI) on the cold streams that feed massive halos at high redshift, generalizing our earlier results to include the effects of radiative cooling and heating from a UV background, using analytic models and high resolution idealized simulations. We currently do not consider self-shielding, thermal conduction or gravity. A key parameter in determining the fate of the streams is the ratio of the cooling time in the turbulent mixing layer which forms between the stream and the background following the onset of the instability,  $t_{\text{cool,mix}}$ , to the time in which the mixing layer expands to the width of the stream in the non-radiative case,  $t_{\text{shear}}$ . This can be converted into a critical stream radius,  $R_{\text{s,crit}}$ , such that  $R_{\text{s}}/R_{\text{s,crit}} = t_{\text{shear}}/t_{\text{cool,mix}}$ . If  $R_{\text{s}} < R_{\text{s,crit}}$ , the non-linear evolution proceeds similarly to the non-radiative case studied by Mandelker et al. (2019a). If  $R_{\text{s}} > R_{\text{s,crit}}$ , which we find to almost always be the case for astrophysical cold streams, the stream is not disrupted by KHI. Rather, background mass cools and condenses onto the stream, and can increase the mass of cold gas by a factor of  $\sim 3$  within 10 stream sound crossing times. The mass entrainment induces thermal energy losses from the background and kinetic energy losses from the stream, which we model analytically. Roughly half of the dissipated energy is radiated away from gas with  $T < 5 \times 10^4$  K, suggesting much of it will be emitted in Ly $\alpha$ .

**Key words:** cosmology — galaxies: evolution — galaxies: formation — hydrodynamics — instabilities

## 1 INTRODUCTION

Understanding how galaxies acquire fresh gas to fuel ongoing star formation is one of the most important outstanding issues in the field of galaxy formation. This is particularly acute during the peak phase of galaxy formation, at  $z \sim (1 - 4)$ . During this epoch, massive galaxies of  $\sim 10^{11} M_{\odot}$  in baryons are observed to have star-formation rates (SFRs) of  $\sim 100 M_{\odot} \text{ yr}^{-1}$ , with short gas depletion times of  $t_{\text{dep}} \sim 100$  Myr (Genzel et al. 2006; Förster Schreiber et al. 2006; Elmegreen et al. 2007; Genzel et al. 2008; Stark et al. 2008). According to the standard  $\Lambda$ CDM cosmological model, such galaxies are predicted to reside in dark matter halos with virial mass  $M_{\text{v}} \gtrsim 10^{12} M_{\odot}$  (Dekel et al. 2009; Wechsler & Tinker

2018; Behroozi et al. 2019). Such halos are predicted to support a stable accretion shock near the virial radius,  $R_{\text{v}}$ , such that the gas within their circumgalactic medium (CGM) has temperatures of order the virial temperature,  $T_{\text{v}} \sim 10^6$  K, and cooling times of order the Hubble time (Rees & Ostriker 1977; White & Rees 1978; Birnboim & Dekel 2003). While the cooling time becomes shorter near the halo centre, it is unclear whether this can result in cooling flows capable of sustaining the high SFRs, which are comparable to the predicted cosmological accretion rate of gas onto the halos (Dekel et al. 2009). Since these star-forming galaxies appear to be extended rotating disks, it is also unlikely that mergers are responsible for driving the cold gas towards the galaxies (Genzel et al. 2006; Shapiro et al. 2008; Förster Schreiber et al. 2009; Wisnioski et al. 2015; Simons et al. 2019).

In the contemporary picture of galaxy formation,

\* E-mail: nir.mandelker@yale.edu

such massive galaxies at high redshift are fed by narrow streams of dense gas which trace cosmic web filaments (Dekel & Birnboim 2006; Dekel et al. 2009). Owing to their high densities and short cooling times, the gas in these streams does not shock, maintains a temperature of  $T_s \gtrsim 10^4$  K, and is thought to be able to penetrate through the hot CGM and reach the central galaxy in roughly a virial crossing time. This is commonly referred to as the cold-stream model of galaxy formation. Such cold streams are ubiquitous in cosmological simulations of galaxy formation (e.g. Kereš et al. 2005; Ocvirk, Pichon & Teyssier 2008; Dekel et al. 2009; Ceverino, Dekel & Bournaud 2010; Faucher-Giguère, Kereš & Ma 2011; van de Voort et al. 2011; Harford & Hamilton 2011), where they are found to supply the halo with gas at rates comparable both to the predicted cosmological accretion rate and the observed SFR, implying that a significant fraction of the gas must reach the central galaxy (Dekel et al. 2009, 2013). Their narrow size makes the streams difficult to directly detect observationally. However, numerous studies of the CGM around high-redshift massive galaxies, in both absorption (Fumagalli et al. 2011; Goerdt et al. 2012; van de Voort et al. 2012; Bouché et al. 2013, 2016; Prochaska, Lau & Hennawi 2014) and emission (Steidel et al. 2000; Matsuda et al. 2006, 2011; Cantalupo et al. 2014; Martin et al. 2014a,b, 2019; Borisova et al. 2016; Fumagalli et al. 2017; Leclercq et al. 2017; Arrigoni Battaia et al. 2018) reveal large quantities of cold gas with spatial and kinematic properties consistent with predictions for cold streams.

Despite the success of the cold-stream model, the evolution of streams in the CGM is still widely disputed. Different cosmological simulations make different predictions regarding whether or not the streams remain coherent and penetrate all the way to the central galaxy, how much of their energy is dissipated within the halo and how much radiation this dissipation produces, and what effects these may have on the thermal and morphological properties of the gas that eventually joins the galaxy. The latter is particularly important for the growth of galactic disks, as the streams are thought to play a key role in the buildup of angular momentum in disk galaxies (Pichon et al. 2011; Kimm et al. 2011; Stewart et al. 2011, 2013; Codis et al. 2012; Danovich et al. 2012, 2015).

Some of the differences between various simulations have been attributed to different numerical methods. For instance, simulations using the moving mesh code AREPO (Springel 2010; Vogelsberger et al. 2012) suggest that streams heat-up and dissolve at  $\gtrsim 0.5R_v$  (Nelson et al. 2013), while comparable Eulerian AMR (Ceverino, Dekel & Bournaud 2010; Danovich et al. 2015) and Lagrangian SPH (Kereš et al. 2005; Faucher-Giguère et al. 2010) simulations find that the streams remain cold and collimated until  $\sim 0.25R_v$ . However, since none of the aforementioned simulations are able to properly resolve the streams

in the outer halo, the interpretation of these results is uncertain. The resolution in most state-of-the-art simulations is adaptive in a quasi-Lagrangian sense, such that the effective mass resolution is fixed. Consequently, the spatial resolution becomes very poor in the low density CGM near the virial radius, with typical cell sizes of several hundred pc to kpc scales (e.g. Nelson et al. 2016). This is comparable to the stream width itself, which is expected to be of order a few kpc (Padnos et al. 2018; Mandelker et al. 2018). Therefore, current cosmological simulations cannot resolve instabilities at smaller scales which are critical to properly model the detailed evolution of cold streams. While several groups have recently introduced new methods to better resolve the CGM (Hummels et al. 2018; Corlies et al. 2018; Peeples et al. 2019; Suresh et al. 2019; van de Voort et al. 2019), these have focused on less massive galaxies, and have not yet been used to study cold streams.

As an alternative to cosmological simulations, several recent studies have turned to analytic models and idealized, high-resolution numerical simulations to study the evolution of cold streams. In a series of papers, Mandelker et al. (2016); Padnos et al. (2018) and Mandelker et al. (2019a) (hereafter M16; P18; and M19 respectively) studied the Kelvin-Helmholtz Instability (KHI) of a dense stream moving supersonically through a tenuous background in the linear (M16) and non-linear (P18; M19) regimes. These studies were purely hydrodynamical in nature, neglecting additional physical processes such as gravity, radiative cooling and heating, or magnetic fields. They found that sufficiently narrow streams should completely disintegrate in the CGM prior to reaching the central galaxy. The smallest radius which would allow a stream to survive for a virial crossing time ranged from  $(0.005 - 0.05)R_v$ , with denser and faster streams having smaller critical radii for disruption (M19). They also found that KHI caused streams to decelerate, and estimated that for typical stream parameters between  $(10 - 50)\%$  of the gravitational potential energy gained by inflow down the dark-matter halo potential from  $R_v$  to  $0.1R_v$  can be dissipated in the CGM (M19). This may explain why some cosmological simulations find that streams maintain a roughly constant inflow velocity within the halo, rather than accelerate due to gravity (Dekel et al. 2009; Goerdt & Ceverino 2015).

Following up on these studies, several other works have used similar idealized methods to investigate the impacts of additional physics such as self-gravity (Aung et al. 2019) or magnetic fields (Berlok & Pfrommer 2019b) on the evolution of cold streams. Others have addressed more specific questions, such as the impact of KHI on the density distribution within streams (Vossberg, Cantalupo & Pezzulli 2019), or the impact of a smooth transition between the stream and the background on the linear growth rate of KHI (Berlok & Pfrommer 2019a), while still only considering adiabatic hydrodynamics. We comment on the results of these studies in §5 below.

While the aforementioned studies have been

extremely comprehensive, none have included radiative cooling or heating, which is the focus of the present study. Cooling can have a strong influence on KHI in both the linear and non-linear regimes (Massaglia et al. 1992, 1996; Bodo et al. 1993; Vietri, Ferrara & Miniati 1997; Rossi et al. 1997; Hardee & Stone 1997; Stone, Xu & Hardee 1997; Xu, Hardee & Stone 2000; Micono et al. 2000), and can either enhance or inhibit the growth rates depending on the cooling function. Additionally, studies of turbulent mixing layers, such as those formed as the result of KHI, show that cooling can qualitatively alter their evolution (Gronke & Oh 2018, 2020; Ji, Oh & Masterson 2019, hereafter G18; G20; and J19 respectively; Li, Bryan & Quataert 2019). This has been shown to significantly extend the lifetime of cool clouds traveling through a hot background due to condensation of hot gas onto the cloud tail. This process may also be important for the evolution of cold streams (see §2). Finally, explicit treatment of radiative processes is necessary in order to address one of the key open questions regarding cold streams, namely whether the dissipation of their energy in the CGM is capable of powering the Ly $\alpha$  emission of observed Ly $\alpha$  blobs. These have typical luminosities of  $\sim 10^{43}$  erg s $^{-1}$  and sizes of  $\sim (50 - 100)$  kpc (Steidel et al. 2000; Matsuda et al. 2006, 2011). As noted above, M19 found that streams can dissipate up to 50% of the gravitational energy gained by flowing down the halo potential due to KHI. If this energy is radiated away as Ly $\alpha$  then the resulting luminosities would be consistent with Ly $\alpha$  blobs (Dijkstra & Loeb 2009; Goerdt et al. 2010; Faucher-Giguère et al. 2010). However, since M19 did not include radiative cooling, the amount of energy which would be radiated away, as opposed to heating the stream or the background, remained unclear.

The remainder of this paper is organized as follows. In §2 we assess when cooling may be important for the evolution of cold streams by comparing the results of M19 regarding stream disruption and deceleration due to non-radiative KHI with recent results on the evolution of radiative turbulent mixing layers. In §3 we introduce a suite of numerical simulations used to study stream evolution. In §4 we present the results of our numerical analysis and compare these to our analytic predictions. In §5 we discuss the potential effects of additional physics not included in our current analysis. We summarize our conclusions in §6.

## 2 THEORETICAL FRAMEWORK

In this section, we begin in §2.1 by reviewing the main aspects of non-linear KHI in cylindrical streams without radiative cooling, in particular the formation of a turbulent mixing layer in between the two fluids. We continue in §2.2 by reviewing some general properties of turbulent mixing layers with and without radiative cooling. Finally, in §2.3, we use the previous two subsections to predict when cooling will be important in the non-linear evolution of KHI in cold streams.

### 2.1 Non-Radiative KHI in Cylindrical Streams

We focus here on the results of M19, who studied the non-linear evolution of KHI in a dense cylinder moving through a static and dilute background, expanding upon earlier work by M16 and P18. This system is characterized by two dimensionless parameters, the Mach number of the flow with respect to the sound speed in the background,  $M_b = V_s/c_b$ , and the density contrast between the stream and the background,  $\delta = \rho_s/\rho_b$ . If the stream and the background are in pressure equilibrium, the Mach number with respect to the sound speed in the stream is  $M_s = V_s/c_s = \delta^{1/2}M_b$ . The stream radius is  $R_s$ .

We begin by noting that there are two qualitatively different modes of KHI. *Surface modes*, as their name suggests, are initially concentrated near the interface between the two fluids, and propagate into both fluids. In the early non-linear stages of evolution, they display the familiar cat's eye vortex morphology commonly associated with textbook KHI (e.g. Chandrasekhar 1961). *Body modes*, which are relevant at high Mach number flows where  $V_s > (c_s + c_b)$ , are caused by sound waves propagating inside the stream and being reflected off its boundaries while undergoing constructive interference. This causes a global, large scale, deformation of the stream, while leaving the interface itself relatively unperturbed until the final stages of stream disruption. In two dimensions, where the stream is not a cylinder but rather a planar slab confined to the region  $-R_s < x < R_s$  while flowing along the  $z$  direction, surface modes stabilize once  $M_b$  is larger than a critical value of order unity, leaving only unstable body modes. Therefore, the distinction between these two modes is critical (M16; P18). However, in three dimensional cylinders, surface modes with sufficiently large azimuthal wave-numbers,  $m = 2\pi R_s/\lambda_\varphi$ , are always unstable.<sup>1</sup> Body modes, which evolve on longer timescales than surface modes, thus rarely manifest in practice (M19). We therefore restrict the following discussion to surface modes.

The non-linear evolution of KHI surface modes is characterized by the formation of a turbulent shear layer in between the two fluids. This layer forms at the initial interface between the fluids and expands into both fluids, growing by the merger of eddies which drives power towards larger and larger scales. At the same time, the largest eddies break up and transfer power towards smaller scales, generating turbulence. The width of the shear layer as a function of time can be well approximated by

$$h(t) = \alpha V_s t, \quad (1)$$

where the dimensionless growth rate,  $\alpha$ , can be approximated as (Dimotakis 1991)

$$\alpha \simeq 0.21 \times [0.8 \exp(-3M_{\text{tot}}^2) + 0.2], \quad (2)$$

<sup>1</sup> The same is true for planar slabs in three dimensions, where surface modes with sufficiently large wavenumbers perpendicular to the flow yet within the slab plane are always unstable.

with  $M_{\text{tot}} = V_s/(c_s + c_b)$ . This approximation is an excellent fit for 2d planar slabs and for 3d cylinders at early times. At late times, once  $h \sim R_s$ , eq. (1) can still describe shear layer growth in 3d cylinders with a modified value of  $\alpha$ , which differs from eq. (2) by a factor of  $\lesssim 2$  (M19).

The shear layer expands asymmetrically into the stream and the background, due to their different densities. The stream penetration depth into either fluid can be shown to be

$$h_s(t) = \frac{1}{1 + \sqrt{\delta}} h(t), \quad h_b(t) = \frac{\sqrt{\delta}}{1 + \sqrt{\delta}} h(t), \quad (3)$$

such that  $h = h_s + h_b$ . Stream disruption was said to occur when  $h_s = R_s$  at time

$$t_{\text{dis}} = \frac{(1 + \sqrt{\delta}) R_s}{\alpha V_s}. \quad (4)$$

However, in Aung et al. (2019) it was found that when comparing the timescale for KHI induced stream disruption to the timescale for gravitational instability induced stream fragmentation, the relevant KHI timescale was that for which  $h = R_s$ , namely when the total width of the shear layer exceeds the stream radius. This is sensible, because KHI is driven by the presence of a contact discontinuity between the fluids, which disappears once  $h \simeq R_s$ . This is also the time when shear layer growth in 3d cylinders begins to deviate from eq. (2) (M19). This occurs at time

$$t_{\text{shear}} = \frac{R_s}{\alpha V_s}. \quad (5)$$

An additional important timescale is the stream sound crossing time,

$$t_{\text{sc}} = \frac{2R_s}{c_s}. \quad (6)$$

As the shear layer expands into the background, it entrains more and more background mass which shares the initial stream momentum. This causes the stream fluid in the shear layer to decelerate, and its velocity as a function of time is well fit by (M19)

$$V_s(t) = \frac{V_{s,0}}{1 + t/t_{\text{dec}}}, \quad (7)$$

with  $V_{s,0}$  the initial velocity of the stream, and

$$t_{\text{dec}} = \frac{(1 + \sqrt{\delta})(\sqrt{1 + \delta} - 1) R_s}{\alpha \sqrt{\delta} V_{s,0}}, \quad (8)$$

the time when the entrained background mass equals the initial stream mass.

Since the deceleration is induced by mass entrainment and momentum conservation, we have that  $mV = m_0 V_0 = \text{const}$ , with  $m$  the total mass per unit length, stream plus background, that is flowing and  $V$  is the characteristic velocity of the flow. Since the total kinetic energy per unit length associated with this

laminar flow is  $E_k \sim 0.5mV^2 \sim E_{k,0}V/V_0$ , the bulk kinetic energy decreases with time as

$$E_k(t) = \frac{E_{k,0}}{1 + t/t_{\text{dec}}}, \quad (9)$$

similar to the stream velocity. This dissipated energy can be converted into turbulence or into thermal energy in either the stream or the background, or be advected away from the stream via sound waves. If the gas can cool, some fraction of it will be radiated away.

## 2.2 Turbulent Mixing Layers

Radiatively cooling turbulent mixing layers have received much interest in the literature lately, primarily in the context of cold clouds moving through a hot medium either in the ISM or CGM (G18; G20; J19). It has been found that cooling in these layers can have a profound impact on the survival of such clouds. Since KHI surface modes in cylindrical streams also form a turbulent mixing layer, it is likely that radiative cooling can have a similar influence on stream survival. We here summarize some of the general properties of radiative turbulent mixing layers, modifying them for cylindrical rather than initially spherical or planar geometry where relevant (and stating so explicitly). We apply these results to cold streams in the next subsection.

The general structure of turbulent mixing layers was studied analytically by Begelman & Fabian (1990) and recently revisited by G18. At the interface between hot and cold gas in pressure equilibrium, with densities and temperatures  $\rho_{b,s}$  and  $T_{b,s}$ , respectively, KHI will cause a turbulent mixing layer to develop. By estimating the mass entrainment rates of hot and cold gas into the mixing layer, they derive the mean density and temperature of the mixing layer to be

$$\rho_{\text{mix}} \simeq (\rho_b \rho_s)^{1/2} = \delta^{-1/2} \rho_s, \quad (10)$$

$$T_{\text{mix}} \simeq (T_b T_s)^{1/2} = \delta^{1/2} T_s. \quad (11)$$

An important timescale in determining the dynamics of such systems is the radiative cooling time of the mixing layer,

$$t_{\text{cool, mix}} = \frac{k_B T_{\text{mix}}}{(\gamma - 1) n_{\text{mix}} \Lambda(T_{\text{mix}})}, \quad (12)$$

where  $\gamma$  is the adiabatic index of the gas,  $k_B$  is Boltzmann's constant,  $n_{\text{mix}}$  is the particle number density in the mixing region, and  $\Lambda(T_{\text{mix}})$  is the cooling function evaluated at  $T_{\text{mix}}$ .

In their study of the evolution of cold clouds moving supersonically in a hot atmosphere, G18 and G20 find qualitatively different results depending on whether  $t_{\text{cool, mix}}$  is larger or smaller than the cloud-crushing time,  $t_{\text{cc}} \simeq \delta^{1/2} r_{\text{cl}}/V_{\text{cl}}$ , where  $r_{\text{cl}}$  is the cloud radius and  $V_{\text{cl}}$  is its velocity (though see Li et al. 2019 for a different formalism involving the cooling time in the hot medium).  $t_{\text{cc}}$  is the characteristic timescale for the cloud to be destroyed by a combination of KHI, Rayleigh-Taylor instabilities, and ram-pressure

shocks crossing the cloud. If  $t_{\text{cool,mix}} > t_{\text{cc}}$  then while the cloud lifetime is extended by a factor of a few compared to the non-radiative case, it is ultimately still disrupted and mixed into the background within a few  $t_{\text{cc}}$  (Scannapieco & Brüggén 2015; Schneider & Robertson 2017; G18). However, if  $t_{\text{cool,mix}} < t_{\text{cc}}$ , then the cloud not only survives but actually grows in mass by entraining background material (Armillaotta, Fraternali & Marinacci 2016; Armillaotta et al. 2017; G18; G20; Li et al. 2019). In the former case, KHI transports cold gas from the cloud through the turbulent mixing layer and mixes it into the background. In the latter case, the flow through the turbulent mixing layer is driven by pressure gradients formed as a result of radiative cooling within the layer, and the net result is background gas cooling and condensing onto the cold cloud (J19; G20).

The accretion rate of background gas onto the cold cloud can be written as

$$\dot{m} \simeq \rho_b A v_{\text{mix}}, \quad (13)$$

where  $A$  is the effective surface area of the mixing layer and  $v_{\text{mix}}$  is the characteristic velocity of material flowing through the mixing layer. In the case of initially spherical clouds, the surface area grows much larger than  $4\pi r_{\text{cl}}^2$  due to the formation of an extended tail on the trailing end. It can be shown that in this case  $A \propto r_{\text{cl}}^2 \delta$  (G20). However, this will not be the case for an initially cylindrical stream since there is no tail formation. In this case, the surface area will scale as

$$A \sim 2\pi R_s L \quad (14)$$

where  $L$  is the length of the stream. For an infinite stream,  $m$  and  $A$  can be taken per unit length. Note that in practice, the actual surface area of the mixing layer can be much larger, due to small scale fractal structures that develop in the turbulent mixing zone. Such small scale structures are difficult to account for analytically, and in the cloud simulations of G20, their total surface area remains unconverged with 64 cells across the cloud radius. Numerically evaluating the total surface area in our simulations is beyond the scope of this paper. Rather, similarly to G20, we use eq. (14) as an effective surface area for the mixing layer on the large scales which drive the mixing. We comment more on this below.

The mixing velocity,  $v_{\text{mix}}$ , scales as (G20)

$$v_{\text{mix}} \propto c_s (t_{\text{cool,s}}/t_{\text{sc}})^{-1/4}, \quad (15)$$

where  $t_{\text{cool,s}}$  is the cooling time in the cold phase. The scaling  $v_{\text{mix}} \propto t_{\text{cool}}^{-1/4}$  was first seen in the turbulent mixing layer simulations of J19, and was later explained by G20. For completeness, we repeat the main arguments of the derivation here, referring readers to J19 and G20 for a more in depth discussion. The basic idea rests on two assumptions. First, that the growth of the mixing layer can be modeled as a turbulent diffusion process with the size of the mixing layer,  $H$ , determined by equating the diffusion and cooling timescales. This yields  $H \propto (r_{\text{cl}} c_s t_{\text{cool}})^{1/2}$ . Second, that within the mixing layer, pressure fluctuations are generated by

cooling at a rate  $\delta\dot{P} \sim P/t_{\text{cool}}$ , damped by sound waves at a rate  $\delta\dot{P} \sim -\delta P/t_{\text{sc,H}}$ , and that these balance each other in steady-state. This yields  $\delta P/P \sim t_{\text{sc,H}}/t_{\text{cool}} \sim H/(c_s t_{\text{cool}}) \propto [r_{\text{cl}}/(c_s t_{\text{cool}})]^{1/2} \sim (t_{\text{sc}}/t_{\text{cool}})^{1/2}$ . In this case, the inflow into the mixing layer from large scales is dominated by a quasi-isobaric cooling flow obeying a Bernoulli-like constraint  $P + \rho v_{\text{mix}}^2 \sim \text{const}$ , from where it follows that  $v_{\text{mix}}^2 \sim \delta P/\rho$  and hence  $v_{\text{mix}} \sim c_s (t_{\text{sc}}/t_{\text{cool}})^{1/4}$ .

As we will discuss in §2.3, we assume that the stream is in thermal equilibrium with a UV background, so the net cooling time within the stream is infinite. As described above, the cooling time enters the expression for  $v_{\text{mix}}$  through the formation of pressure gradients, which will be largest where the cooling time is minimal. The minimal net cooling time turns out to always occur at roughly  $T \sim 1.5T_s$ , so we hereafter replace  $t_{\text{cool,s}}$  in eq. (15) with  $t_{\text{cool,T}=1.5T_s}$ . This assumption will be validated using numerical simulations in §4.

In the cloud simulations of G20, the amplitude of  $v_{\text{mix}}$  is found to be unconverged with 64 cells across the cloud radius, similar to  $A$ , due to the fractal structure of the mixing layer on small scales. However, eq. (15) is found to be representative of the velocity through the mixing layer on large scales, just as eq. (14) is representative of the surface area on large scales.

Combining eqs. (13)-(15) we obtain an expression for the mass accretion rate onto a cylindrical stream

$$\dot{m} \sim \frac{4}{\delta} \frac{m_0}{t_{\text{sc}}} \left( \frac{t_{\text{cool,1.5T}_s}}{t_{\text{sc}}} \right)^{-1/4} = \text{const}, \quad (16)$$

where  $m_0 = \pi R_s^2 L \rho_s$  is the initial stream mass, and  $t_{\text{sc}}$  is given by eq. (6). Note the additional factor  $\delta^{-1}$  compared to the corresponding expression in G20, due to the different scaling of the surface area,  $A$ , discussed above.

Unlike the surface area of and velocity through the mixing layer,  $A$  and  $v_{\text{mix}}$ , the mass flux through the mixing layer is found to be converged with as few as 8 cells per cloud radius in the simulations of G20. We find the same for our simulations of cylindrical streams (Appendix §A). We interpret this as the result of a turbulent cascade within the mixing layer, whereby the flux of mass and energy towards smaller scales is independent of scale, as in Kolmogorov turbulence. The total mass flux through the mixing layer is thus set by the large scales which drive the mixing, and not the small scales which are dominated by the fractal structure. This justifies our use of eqs. (14) and (15) in the expression for  $\dot{m}$  in eq. (16). In §4 we will validate these assumptions by comparing eq. (16) to simulation results. However, a scale-dependent measurement of  $A$  and  $v_{\text{mix}}$  in our simulations is beyond the scope of this paper, and left for future work which will characterise the nature of the turbulence in the stream-background interface.

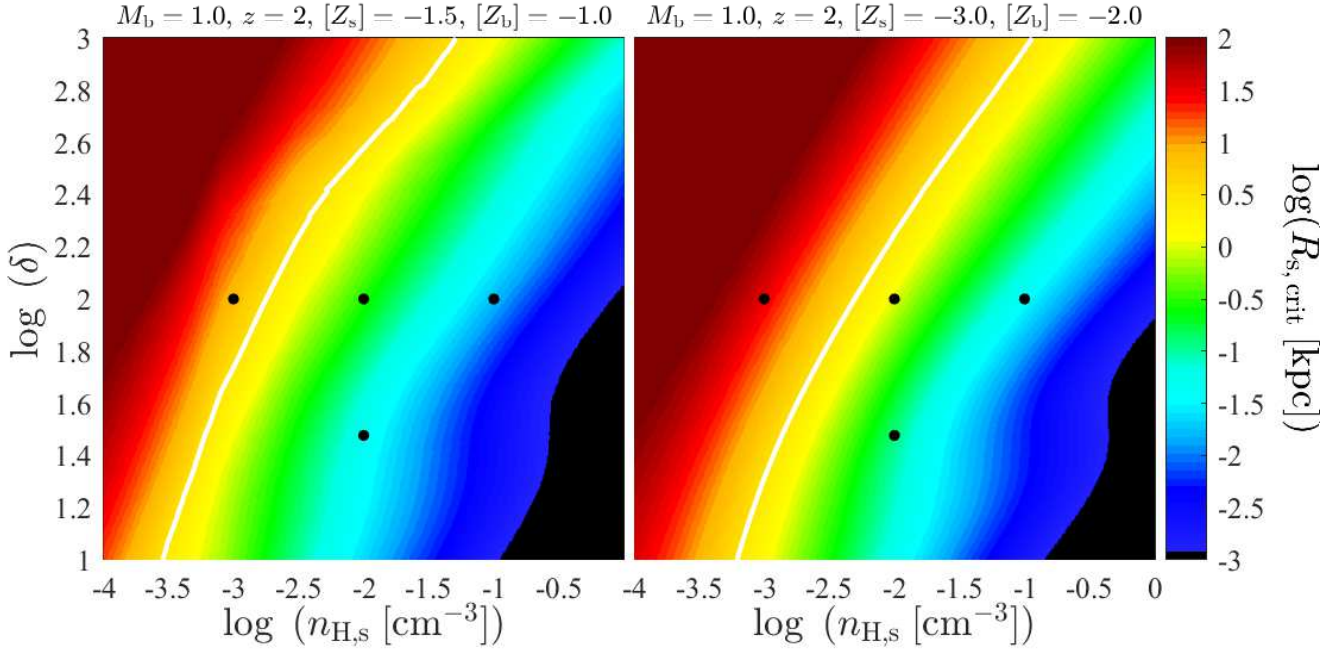


**Figure 1.** Critical stream radius for which  $t_{\text{cool,mix}} = t_{\text{shear}}$ , as a function of stream density,  $n_{\text{H,s}}$ , and density contrast with respect to the halo,  $\delta$ , following eq. (17). The stream temperature is evaluated by assuming thermal equilibrium between the stream and a Haardt & Madau (1996) UV background at  $z = 2$ . We further assume  $M_b = 1$  and evaluate  $\alpha$  from eq. (2). The left (right) panels represent upper and lower limits for the metallicity in the stream and background, with assumed values listed in each panel. The white contours mark  $R_{\text{s,crit}} = 3$  kpc, the fiducial value of  $R_s$  used in our simulations. Black points mark  $(n_{\text{H,s}}, \delta)$  values used in our simulations.

### 2.3 The Importance of Cooling for Cold Stream Stability

In the case of a cylindrical stream in a shear flow, the time when the shear layer expands to the size of the stream,  $t_{\text{shear}}$  (eq. 5), can be considered analogous to the cloud crushing time. Therefore, motivated by the results discussed above, we speculate that when  $t_{\text{cool,mix}} \gtrsim t_{\text{shear}}$ , the non-linear evolution of KHI in streams will be similar to the non-radiative case, where streams disrupt and mix into the background. However, if  $t_{\text{cool,mix}} \lesssim t_{\text{shear}}$ , cold streams may survive for much longer timescales and even grow in mass. Equating  $t_{\text{cool,mix}} = t_{\text{shear}}$  gives a critical stream radius,

$$R_{\text{s,crit}} \simeq 0.3 \text{ kpc } \alpha_{0.1} \delta_{100}^{3/2} M_b \frac{T_{\text{s},4}}{n_{\text{s},0.01} \Lambda_{\text{mix},-22.5}}, \quad (17)$$

where  $T_{\text{s},4} = T_{\text{s}}/10^4 \text{ K}$ ,  $n_{\text{s},0.01} = n_{\text{s}}/0.01 \text{ cm}^{-3}$ ,  $\Lambda_{\text{mix},-22.5} = \Lambda(T_{\text{mix}})/10^{-22.5} \text{ erg s}^{-1} \text{ cm}^3$ ,  $\delta_{100} = \delta/100$ , and  $\alpha_{0.1} = \alpha/0.1$ . Since  $t_{\text{cool,mix}}/t_{\text{shear}} = (R_{\text{s}}/R_{\text{s,crit}})^{-1}$ , streams with  $R_{\text{s}} \gtrsim R_{\text{s,crit}}$  are expected to grow in mass rather than dissolve. We note, however, that the critical ratio of  $t_{\text{cool,mix}}/t_{\text{shear}}$  need not be precisely unity, yielding some uncertainty in the precise normalization of  $R_{\text{s,crit}}$ . We will examine this further below using numerical simulations.

In Fig. 1, we present  $R_{\text{s,crit}}$  as a function of the Hydrogen number density in the stream<sup>2</sup>  $n_{\text{H,s}}$ , and the

density contrast,  $\delta$ . To evaluate the stream temperature, we assume the stream to be in thermal equilibrium with a  $z = 2$  Haardt & Madau (1996) UV background. In particular, we are ignoring the possibility that the streams may be self-shielded. This equilibrium temperature varies with density, but is roughly  $T_{\text{s},4} \sim (1 - 2)$ . We assume  $M_b = 1$  and use eq. (2) to evaluate  $\alpha$ . The cooling curve depends on the metallicity in the stream and the background. These are not well constrained, but simulations suggest that  $Z_{\text{s}}$  can range from  $\sim 10^{-3}$  to a few percent of the solar value, while  $Z_{\text{b}}$  ranges from  $\sim (0.01 - 0.1)Z_{\odot}$  (e.g. Goerdt et al. 2010; Fumagalli et al. 2011; van de Voort & Schaye 2012; Roca-Fàbrega et al. 2019). To bracket these two extremes, we show on the left-hand side of Fig. 1 a model with  $Z_{\text{s}} = 0.03Z_{\odot}$  and  $Z_{\text{b}} = 0.1Z_{\odot}$ , while on the right-hand side we assume  $Z_{\text{s}} = 0.001Z_{\odot}$  and  $Z_{\text{b}} = 0.01Z_{\odot}$ . In each case we assume the metallicity in the mixing region is  $Z_{\text{mix}} = (Z_{\text{s}}Z_{\text{b}})^{1/2}$ , in accordance with eq. (10).

Analytic considerations and cosmological simulations suggest that for cold streams feeding  $\sim 10^{12}M_{\odot}$  halos at redshifts  $z = (2 - 3)$ ,  $n_{\text{H,s}} \sim (0.001 - 0.1)$  (Goerdt et al. 2010),  $\delta \sim (30 - 300)^3$  and

Hydrogen mass fraction of  $X = 0.76$  and a mean molecular weight of  $\mu \sim 0.59$ , the total number density used in eq. (17) is related to the Hydrogen number density by  $n_{\text{s}} \simeq 2.2n_{\text{H,s}}$ .

<sup>3</sup> Note that this is slightly higher than the typical range of  $\delta = (10 - 100)$  assumed in M16, P18, and M19

<sup>2</sup> For fully ionized gas with primordial composition, i.e. a



$M_b \sim (0.5 - 2.0)$  (P18; M19). In this range, we have  $R_{s,\text{crit}} \sim (0.01 - 100)$  kpc, spanning four orders of magnitude, increasing as either the density or metallicity in the stream or the background decrease. While the actual stream radii are not well constrained, analytic considerations predict (P18)

$$R_s/R_v \sim (0.01 - 0.1) (n_{s,0.01} M_b)^{-1/2}, \quad (18)$$

with a typical value of  $\sim 0.06$ . The right-hand-side of eq. (18) can be inferred from equations (62) and (68) of P18. The range  $(0.01 - 0.10)$  comes from uncertainties in model parameters (see P18). The virial radius is (e.g. Dekel et al. 2013)

$$R_v \simeq 100 \text{ kpc } M_{12}^{1/3} (1+z)_3^{-1}, \quad (19)$$

with  $M_{12} = M_v/10^{12} M_\odot$  and  $(1+z)_3 = (1+z)/3$ . This implies that in halos with  $M_v \gtrsim 10^{12} M_\odot$  at  $z \sim (2-3)$ , we expect stream radii in the range  $R_s \sim (0.5 - 10)$  kpc  $n_{s,0.01}^{-1/2}$ . This can be smaller or larger than  $R_{s,\text{crit}}$  depending on the stream parameters, though we almost always expect  $R_s > R_{s,\text{crit}}$ .

Note that  $R_s$  in the above discussion refers to the stream radius upon entering the halo at  $r = R_v$ . As the stream penetrates into the halo, its density increases and its radius decreases. For an isothermal halo, we have  $n \propto r^{-2}$  and  $R_s \propto r \propto n^{-1/2}$  while  $\delta$  remains constant (P18;M19). Combined with eq. (18), we have that  $R_s \propto n^{-1}$ , similar to  $R_{s,\text{crit}}$ . Thus, if  $R_s > R_{s,\text{crit}}$  near  $R_v$ , it is likely to remain so throughout the halo. In a companion paper (Mandelker et al. 2020), we present a more detailed analytic model for stream evolution within dark matter halos.

The white contour in each panel of Fig. 1 marks  $R_{s,\text{crit}} = 3$  kpc, which is the fiducial stream radius in the simulations described in §3 below. In the region of  $(n_{H,s}, \delta)$  space to the right of the curve, which represents most of the expected parameter range for cold streams,  $t_{\text{cool,mix}} < t_{\text{shear}}$ , and the non-linear behaviour of the turbulent mixing zone between the stream and the background will be dominated by cooling. To the left of the curve, we expect the non-linear behaviour to be qualitatively similar to the non-radiative case described in §2.1. Black points mark  $(n_{H,s}, \delta)$  values used in the simulations described in the next section.

### 3 NUMERICAL METHODS

In this section we describe the details of our simulation code and setup. We use the Eulerian AMR code **RAMSES** (Teyssier 2002), with a piecewise-linear reconstruction using the MonCen slope limiter (van Leer 1977), and an HLLC approximate Riemann solver (Toro, Spruce & Speares 1994). We utilise the standard **RAMSES** cooling module, which accounts for atomic and fine-structure cooling for our assumed metallicity values (see below), as well as photoheating and photoionization from a  $z = 2$  Haardt & Madau (1996) UV background. We do not include self-shielding of dense gas in this work.

#### 3.1 Stream Parameters

We perform a total of 17 simulations exploring 11 combinations of values for the stream Mach number,  $M_b = (0.5, 1.0, 2.0)$ , density contrast,  $\delta = (30, 100)$ , density,  $n_{H,s} = (0.001, 0.01, 0.1) \text{ cm}^{-3}$ , and radius,  $R_s = (0.3, 3, 6, 30)$  kpc. Three of these simulations were repeated with cooling switched off<sup>4</sup>. The full list of simulations can be found in Table 1. All simulations assume metallicity values  $Z_s = 0.03 Z_\odot$  and  $Z_b = 0.1 Z_\odot$ . The equation of state of both fluids is that of an ideal monoatomic gas with adiabatic index  $\gamma = 5/3$ . The initial stream temperature is set to be in thermal equilibrium with the UV background at the assumed stream density, and is typically  $T_s \sim 1.5 \times 10^4 \text{ K}$ . The density in the background is  $n_{H,b} = \delta^{-1} n_{H,s}$  and the temperature is determined by pressure equilibrium by  $T_b/\mu_b = \delta T_s/\mu_s$ , where  $\mu_b \sim \mu_s \sim 0.6$  are the mean molecular weights in the background and stream respectively, determined from the ionization state.

To prevent the hot gas from cooling over long periods of time, we turn off cooling for gas with  $T > T_{\text{max}}$ . In most of our simulations we use  $T_{\text{max}} \gtrsim (T_s T_b)^{1/2}$ . We perform two additional simulations increasing  $T_{\text{max}}$  by a factor  $\sim 4$  (see Table 1) and find our results robust to this choice. This is consistent with the results of G18 and G20 which are shown to be robust to shutting off cooling at  $T > 0.6 T_b$  and not shutting it off at all. As we discuss in §4, this is because most of the emissivity originates in cool gas with  $T \gtrsim T_s$ , as also found in J19 and G20.

We run each of our simulations for 10 stream sound crossing times (eq. 6), saving 15 outputs per sound crossing time. The ratio of halo crossing time,  $t_v = R_v/V_s$ , to stream sound crossing time is

$$\frac{t_v}{t_{\text{sc}}} = \frac{1}{2} \left( \frac{R_s}{R_v} \right)^{-1} \delta^{-1/2} M_b^{-1}. \quad (20)$$

For our simulated parameters, this is  $t_v \sim (0.5 - 6) t_{\text{sc}}$ .

#### 3.2 Simulation Domain, Boundary Conditions, & Resolution

The simulation domain is a cube of side  $L = 32 R_s$ , extending from  $-16 R_s$  to  $16 R_s$  in all directions. We hereafter adopt the standard cylindrical coordinates,  $(r, \varphi, z)$ , where the  $z$  axis corresponds to the stream axis. The stream fluid occupies the region  $r < R_s$  while the background fluid occupies the rest of the domain.

We use periodic boundary conditions at  $z = \pm 16 R_s$ , and outflow boundary conditions, at  $x = \pm 16 R_s$  and  $y = \pm 16 R_s$ , such that gas crossing the boundary is lost from the simulation domain. At these boundaries, the gradients of density, pressure, and velocity are set to 0.

We use a statically refined grid with resolution decreasing away from the stream axis. The highest

<sup>4</sup> Note that the non-radiative simulations are scale free, so the only meaningful parameters are  $M_b$  and  $\delta$ .

Label	$M_b$	$\delta$	$n_{H,s}$ [cm <sup>-3</sup> ]	$R_s$ [kpc]	$T_s$ [10 <sup>4</sup> K]	$T_{\max}$ [10 <sup>4</sup> K]	$m_{\max}$	$t_{\text{cool,mix}}$ [ $t_{\text{shear}}$ ]	$t_{\text{cool,1.5}T_s}$ [ $t_{\text{sc}}$ ]
M0.5_d100	0.5	100	0.01	3	1.51	20	1	0.114	0.0085
M1.0_d100	1.0	100	0.01	3	1.51	20	1	0.097	0.0085
M2.0_d100	2.0	100	0.01	3	1.51	20	1	0.145	0.0085
M0.5_d30	0.5	30	0.01	3	1.51	11	1	0.018	0.0085
M1.0_d30	1.0	30	0.01	3	1.51	11	1	0.016	0.0085
M2.0_d30	2.0	30	0.01	3	1.51	11	1	0.022	0.0085
M1.0_d100_LD	1.0	100	0.001	3	1.76	20	1	2.441	0.6389
M1.0_d100_HD	1.0	100	0.1	3	1.25	20	1	0.006	0.0002
M1.0_d100_HR	1.0	100	0.01	6	1.51	80	1	0.049	0.0042
M1.0_d100_LDHR	1.0	100	0.001	30	1.76	80	1	0.244	0.0639
M1.0_d100_LR	1.0	100	0.01	0.3	1.51	80	1	0.97	0.085
M1.0_d100_HT	1.0	100	0.01	3	1.51	80	1	0.097	0.0085
M1.0_d30_HT	1.0	30	0.01	3	1.51	40	1	0.016	0.0085
M2.0_d100_Hm	2.0	100	0.01	3	1.51	80	4	0.145	0.0085
M0.5_d100_NR	0.5	100	--	--	--	--	--	--	--
M1.0_d100_NR	1.0	100	--	--	--	--	--	--	--
M2.0_d100_NR	2.0	100	--	--	--	--	--	--	--

**Table 1.** Stream parameters in the different simulations. The leftmost column is a label identifying the simulation, specifying the Mach number, the density contrast, and an additional comment. LD means low density (compared to the fiducial  $n_{H,s}$ ), HD means high density, HR means high (large) radius, LR means low (small) radius, HT means high  $T_{\max}$ , Hm means high (large) azimuthal mode numbers  $m$  in the initial perturbations, and NR means non-radiative. Note that the HR, LDHR, LR, and Hm runs also have high  $T_{\max}$ . The next four columns list the control parameters: the Mach number,  $M_b$ , density contrast,  $\delta$ , Hydrogen number density in the stream,  $n_{H,s}$  in cm<sup>-3</sup>, and the stream radius,  $R_s$  in kpc. The next two columns list the stream temperature,  $T_s$  and the temperature above which cooling is shut off,  $T_{\max}$ , both in K. The next column lists the maximal azimuthal mode number,  $m$ , with all modes  $m = 0 - m_{\max}$  present in the initial perturbation spectrum. The final two columns list the ratios  $t_{\text{cool,mix}}/t_{\text{shear}}$  and  $t_{\text{cool,1.5}T_s}/t_{\text{sc}}$  (see eq. (15)). Only the LD simulation has  $t_{\text{cool,mix}}/t_{\text{shear}} > 1$ , placing it in the slow-cooling regime (see Fig. 1).

resolution region is  $\max(|x|, |y|) < 1.5R_s$ , with cell size  $\Delta = R_s/64$ . The cell size increases by a factor of 2 every  $1.5R_s$  in the  $x$  and  $y$ -directions, up to a maximal cell size of  $R_s/4$ . The resolution is uniform along the  $z$  direction, parallel to the stream axis. In the non-radiative case, KHI surface modes are converged at this resolution, both in terms of the cell size and the width of the high-resolution region (M19). Our main results for the radiative case are converged as well (appendix §A).

Note that unlike the simulations presented in M16; P18; M19 and Aung et al. (2019), we do not smooth the interface between the stream and the background, maintaining instead a step function in  $r$ . Such a smooth transition layer is out of thermal equilibrium, and it rapidly cools and condenses onto the stream. Not only does this negate the initial purpose of smoothing, it also creates a weak shock wave that propagates towards the stream axis. While the lack of such a smooth transition makes the simulations susceptible to numerical perturbations on the grid scale, we have verified that these do not change the non-linear behaviour, since in any case we initialize a broad spectrum of perturbation modes (see also P18).

### 3.3 Perturbations

The stream is initialised with velocity  $\mathbf{V}_s = M_b c_b \hat{\mathbf{z}}$ , where  $c_b = (\gamma P_b / \rho_b)^{1/2}$  is the sound speed in the background. The background gas is initialised at rest, with velocity  $\mathbf{V}_b = 0$ .

We then perturb our simulations in a manner very

similar to M19 and Aung et al. (2019). We initialize a random realization of periodic perturbations in the radial component of the velocity,  $v_r = v_x \cos(\varphi) + v_y \sin(\varphi)$ . In practice, we perturb the Cartesian components of the velocity,

$$v_x^{\text{pert}}(r, \varphi, z) = \sum_{j=1}^{N_{\text{pert}}} v_{0,j} \cos(k_j z + m_j \varphi + \phi_j) \times \exp \left[ -\frac{(r - R_s)^2}{2\sigma_{\text{pert}}^2} \right] \cos(\varphi), \quad (21)$$

$$v_y^{\text{pert}}(r, \varphi, z) = \sum_{j=1}^{N_{\text{pert}}} v_{0,j} \cos(k_j z + m_j \varphi + \phi_j) \times \exp \left[ -\frac{(r - R_s)^2}{2\sigma_{\text{pert}}^2} \right] \sin(\varphi). \quad (22)$$

The velocity perturbations are localised on the stream-background interface, with a penetration depth set by the parameter  $\sigma_{\text{pert}}$ , which is  $R_s/16$  in all of our simulations. To comply with periodic boundary conditions, all wavelengths are harmonics of the box length,  $k_j = 2\pi n_j$ , where  $n_j$  is an integer, corresponding to a wavelength  $\lambda_j = 1/n_j$ . Each simulation includes all wavenumbers in the range  $n_j = 2 - 64$ , corresponding to all available wavelengths in the range  $R_s/2 - 16R_s$ . Each wavenumber is also assigned a symmetry mode, represented by the index  $m_j$  in eqs. (21) and (22). For each wavenumber we include both an  $m = 0$  and an  $m = 1$  mode, corresponding to axisymmetric and helical modes, respectively. This yields a total



of  $N_{\text{pert}} = 2 \times 63 = 126$  modes per simulation. In one simulation, M2.0\_d100\_Hm (Table 1), we included modes with  $m = 0, 1, 2, 3, 4$ , yielding a total of  $N_{\text{pert}} = 5 \times 63 = 315$  modes. Each mode is then given a random phase  $\phi_j \in [0, 2\pi)$ . Different realizations with different phases are found to be extremely similar (P18; M19). The amplitude of each mode,  $v_{0,j}$ , is identical, with the rms amplitude normalised to  $0.01c_s$ .

### 3.4 Tracing the Two Fluids

Following P18; M19 and Aung et al. (2019), we use a passive scalar field,  $\psi(r, \varphi, z, t)$ , to track the growth of the shear layer and the mixing of the two fluids. Initially,  $\psi = 1$  and  $0$  in the stream and background respectively. During the simulation,  $\psi$  is advected with the flow such that the density of stream-fluid in each cell is  $\rho_s = \psi\rho$ , where  $\rho$  is the total density in the cell.

The volume-weighted average radial profile of the passive scalar is given by

$$\bar{\psi}(r, t) = \frac{\int_{-L/2}^{L/2} \int_0^{2\pi} \psi(r, \varphi, z, t) r \, d\varphi \, dz}{2\pi r L}. \quad (23)$$

This is used to define the edges of the shear layer around the stream interface,  $r(\bar{\psi} = \epsilon)$  on the background side and  $r(\bar{\psi} = 1 - \epsilon)$  on the stream side, where  $\epsilon$  is an arbitrary threshold. We set  $\epsilon = 0.04$  following M19, though our results are not strongly dependent on this choice. The background-side thickness of the shear layer is then defined as

$$h_b \equiv \max_r r(\bar{\psi} = \epsilon) - R_s, \quad (24)$$

while the stream-side thickness is defined as

$$h_s \equiv R_s - \min_r r(\bar{\psi} = 1 - \epsilon). \quad (25)$$

## 4 SIMULATION RESULTS

In this section we present the results of the numerical simulations described in §3. In §4.1, we discuss the evolution of stream morphology and eventual stream disruption. In §4.2 we discuss mass entrainment onto the stream through the turbulent mixing layer, and subsequent stream deceleration and energy dissipation. In §4.3 we discuss turbulence and heating in the stream driven by the instability. In §4.4 we present results for the total cooling emissivity generated by the instability.

### 4.1 Stream Morphology and Disruption

In Fig. 2 we show a time sequence of the density evolution for simulations M1.0\_d100\_NR (left) and M1.0\_d100 (right). We show a slice through the  $y = 0$  plane of the stream at times  $t = (1, 2, 4, 6, 8)t_{\text{sc}}$ . The differences between the radiative and non-radiative simulations are striking. At  $t = t_{\text{sc}}$ , the density in the non-radiative stream is larger because a shock was able to penetrate to the stream axis, while it was damped in the cooling simulation. However, this is a transient feature, likely influenced by the initial

simulation setup. At all later times the average density in the non-radiative stream is smaller than in the radiative case. In the former, the stream expands into the background and is diluted. By  $t = 8t_{\text{sc}}$ , there is hardly any gas left with density comparable to the initial stream density and the average density along the stream axis is  $\sim 0.2\rho_s$ . On the other hand, the density in the cooling simulation remains high until late times, as stream expansion is suppressed and the background condenses onto the stream. This is expected, since in this case  $t_{\text{cool, mix}} < t_{\text{shear}}$  (Table 1). At  $t = 8t_{\text{sc}}$  the stream has begun to break up, forming small dense clumps near the stream-background interface. These may be due to thermal instabilities in the mixing region, which is pressure confined by the external gas outside this region, leading to fragmentation to the cooling length,  $l_{\text{cool}} = c_s t_{\text{cool}}$  (McCourt et al. 2018). They may also be due to secondary instabilities following the growth of long wavelength modes, seen at  $t = 6$  and  $8t_{\text{sc}}$ , similar to non-linear disruption by body modes seen in M19. This long wavelength mode would have time to manifest in the radiatively cooling simulation, because stream disruption by short-wavelength surface modes is suppressed. A detailed study of the origin of these clumps, and their mass/size distribution, is beyond the scope of this paper and left for future work. For our current purposes, suffice to say that the stream density remains high and that it maintains a relatively collimated structure.

In Fig. 3, we show the evolution of the passive scalar,  $\psi$ , in the same snapshots shown in Fig. 2. In the non-radiative case, the stream expands into the background and stream fluid is found very far from the stream axis. At  $t = 8t_{\text{sc}}$ , we have  $h_b \sim 8.5R_s$ , as defined in eq. (24). On the other hand, there is still a core of unmixed stream fluid with  $\psi \lesssim 1$  near the stream axis, consistent with the fact that for  $(M_b, \delta) = (1.0, 100)$ ,  $t_{\text{dis}} \sim 11t_{\text{sc}}$  (eq. 4). The situation is markedly different in the radiative case. Since  $t_{\text{cool, mix}} < t_{\text{shear}}$ , stream expansion is suppressed and  $h_b$  is only  $\sim 3R_s$  at  $t = 8t_{\text{sc}}$ . However, background material condenses onto the stream and mixes with it, lowering  $\psi$  near the stream axis much faster than in the non-radiative case. By  $t \sim 3t_{\text{sc}}$ ,  $h_s = R_s$ . Based on the definition of stream disruption used in P18, M19, and Aung et al. (2019), this would imply that the stream is disrupted at  $t \sim 3t_{\text{sc}}$ , nearly 4 times faster than the non-radiative case. However, this is clearly not the case as evidenced by the large densities and collimated structure present in the stream until very late times (Fig. 2). This highlights the need for an alternative definition of stream disruption.

In Fig. 4 we show slices of the density and the passive scalar at  $t = 2t_{\text{sc}}$  and  $t = 8t_{\text{sc}}$  for the simulations M1.0\_d100\_LD (left) and M1.0\_d100\_HD (right). In the former,  $t_{\text{cool, mix}} > t_{\text{shear}}$ , while in the latter  $t_{\text{cool, mix}} \ll t_{\text{shear}}$  (Table 1). Based on the arguments outlined in §2.3, the LD case should thus be qualitatively similar to the NR case, while the HD case should be similar to the fiducial simulation. This is indeed the case. In the LD simulation, the stream expands into the background and its density

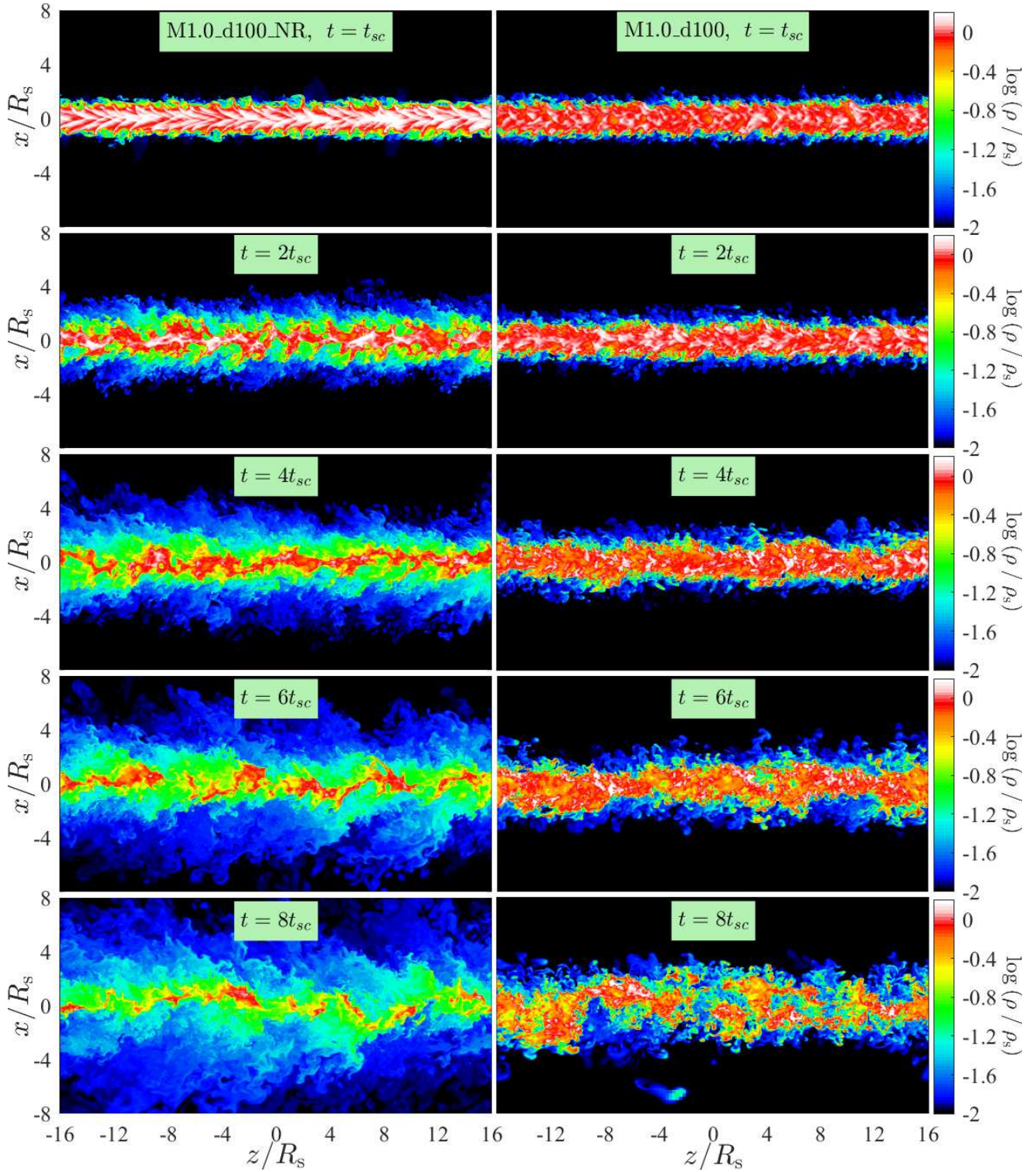


**Figure 2.** Stream evolution without (left) and with (right) radiative cooling. Shown are snapshots of density normalized by the initial stream density,  $\rho/\rho_s$ , in an infinitesimal slice through the  $xz$  plane, an “edge-on” view of the cylinder. The unperturbed initial conditions were  $(M_b, \delta) = (1, 100)$ , the left-hand column shows the NR simulation while the right-hand column shows the fiducial simulation (see Table 1). The snapshot times in units of the stream sound crossing time,  $t_{sc} = 2R_s/c_s$ , are shown in each panel. While the density in the non-radiative case grows smaller as the stream expands into the background and is diluted, the density in the cooling simulation remains high until  $t > 8t_{sc}$ . In this case, stream expansion is suppressed and the background condenses onto the stream since  $t_{cool, mix} < t_{shear}$  (Table 1). Eventually, the stream begins to break up due to thermal instabilities in the turbulent mixing layer, which lead to the formation of small dense clumps near the stream-background interface.



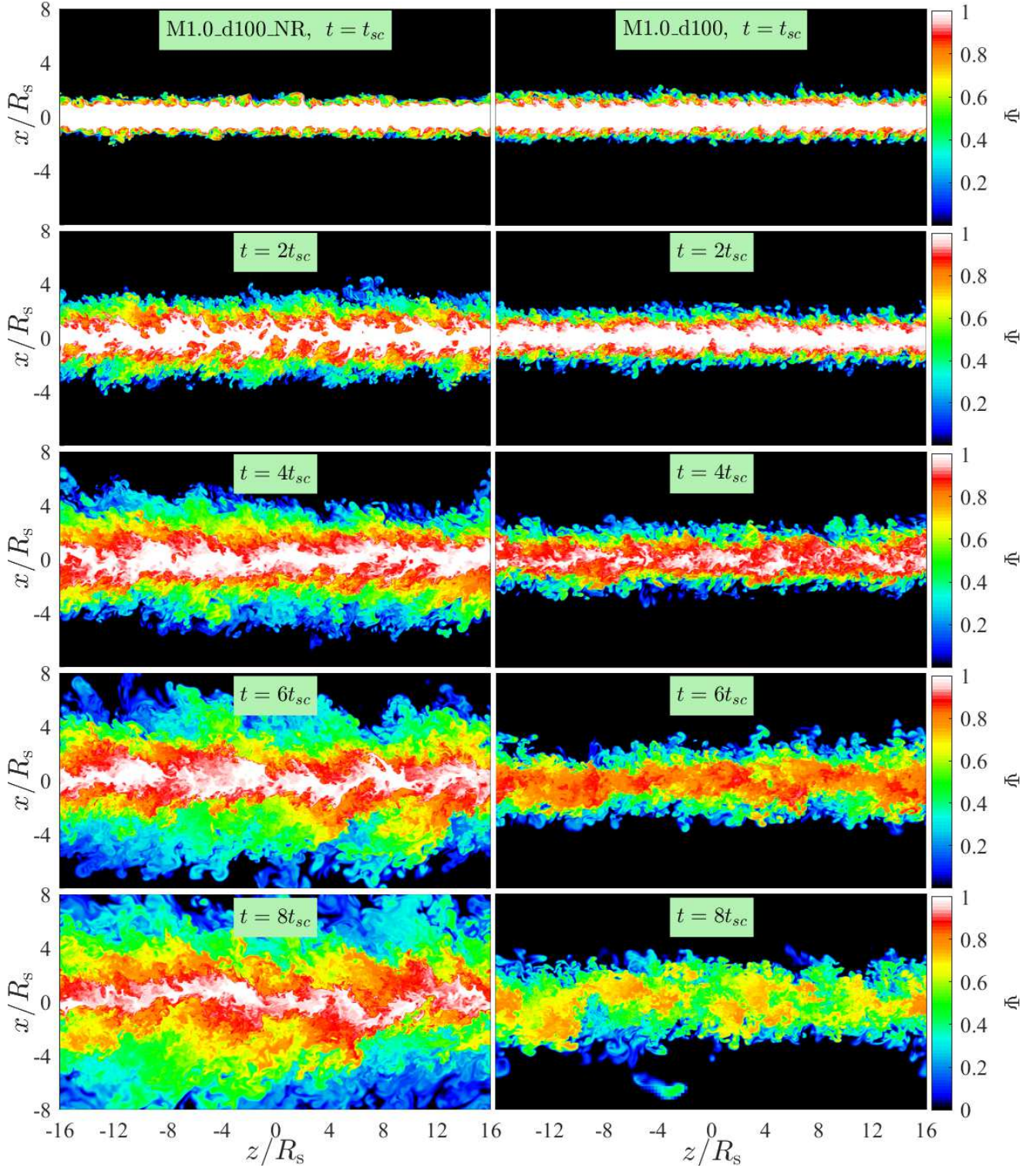


**Figure 3.** Same as Fig. 2, but showing the passive scalar,  $\psi$  (§3.4), rather than the fluid density. In the non-radiative simulation, the stream expands into the background depositing stream fluid far from the initial interface. In the cooling simulation, on the other hand, the background condenses onto the stream and the mixing region is significantly smaller in volume, because  $t_{\text{cool, mix}} < t_{\text{shear}}$ . As a result, the fraction of mixed fluid near the stream centre, with  $\psi < 1$ , increases much faster in the simulation with cooling.

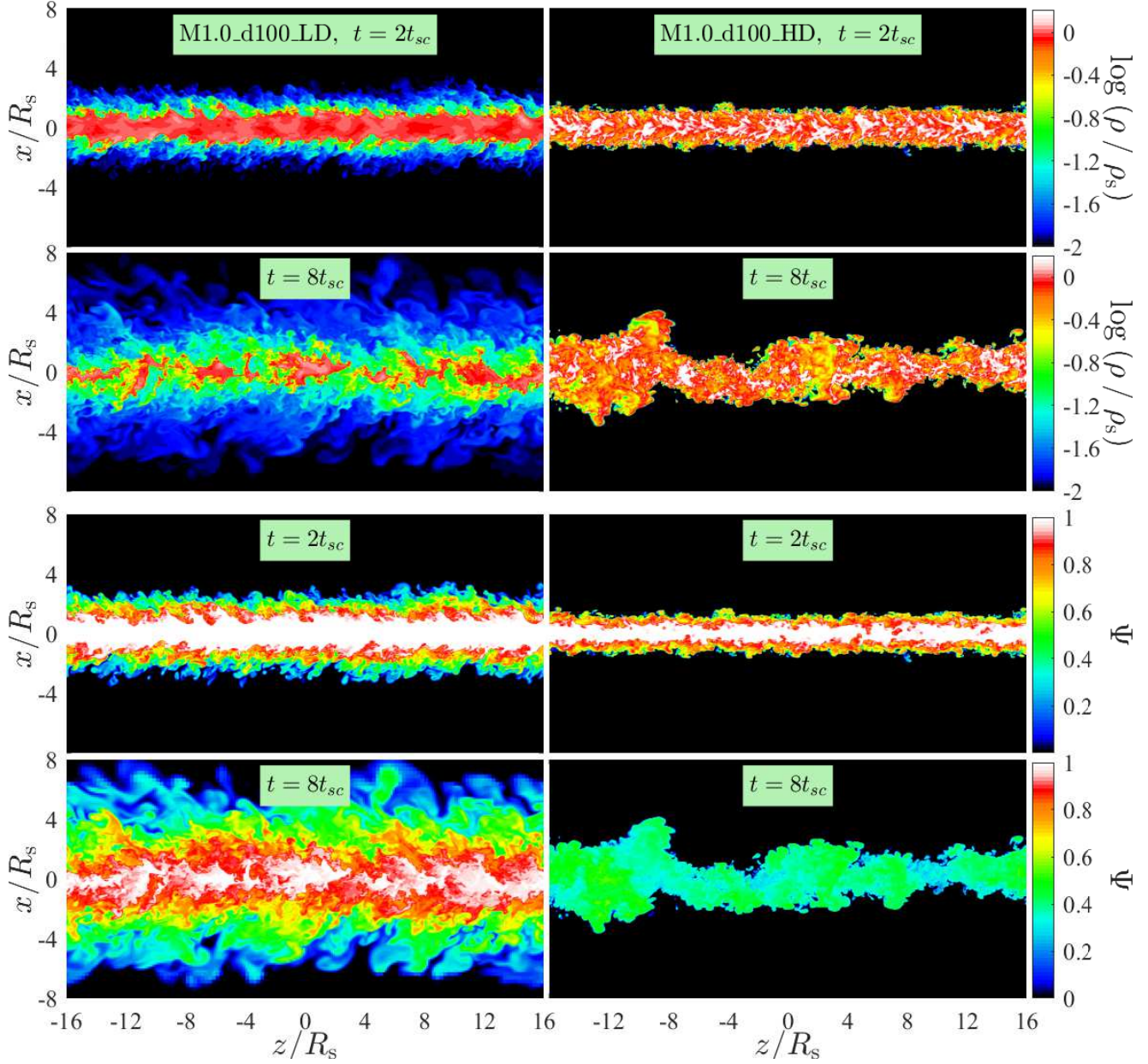


**Figure 4.** Similar to Figs. 2-3, but for the LD (left) and HD (right) simulations with  $(M_b, \delta) = (1.0, 100)$  (see Table 1). The top two rows show the density at  $t = 2t_{sc}$  and  $8t_{sc}$ , while the bottom two rows show the passive scalar at the same times. Since the LD simulation has  $t_{cool, mix} > t_{shear}$ , its behaviour is qualitatively similar to the non-radiative (NR) case shown in Figs. 2-3. In the HD simulation, on the other hand,  $t_{cool, mix}/t_{shear}$  is much smaller than in the fiducial case shown in Figs. 2-3. This leads to a narrower turbulent mixing layer, more condensation of background material onto the stream, higher densities and more mixed fluid near the stream centre.

is diluted. This occurs at a slightly slower rate than in the NR case, with  $h_b \sim 6.5R_s$  at  $t = 8t_{sc}$ , and the average density along the stream axis only half the initial value. This is consistent with simulations of the evolution of cold clouds traveling in a hot background, which find that cooling can delay cloud disruption by a factor of a few when  $t_{cool, mix} > t_{cc}$ , but it does not qualitatively alter the evolution (Scannapieco & Brüggén 2015; Schneider & Robertson 2017; G18). On the other hand, in the HD simulation, the density remains very high and the stream remains highly collimated even at  $t > 8t_{sc}$ . Likewise, the passive

scalar reaches even lower values than in the fiducial case near the stream axis, since the flow of background material through the turbulent mixing region onto the stream is more efficient (eq. 15). Stream breakup into dense clumps appears suppressed compared to the fiducial simulation (bottom right panel of Fig. 2). If such breakup is due to secondary instabilities following the growth of long wavelength modes, these may be stabilized by the more efficient cooling. On the other hand, if the breakup is due to thermal shattering of a pressure confined medium, the clumps may simply be unresolved in this case because the cooling length in the

mixing layer is of the order of a single cell. In this case, we suspect that simulations that resolve the cooling length would produce a similar fragmented structure to that observed in the fiducial case (see Mandelker et al. 2019b). As stated above, the origin and evolution of these small clumps is beyond the scope of the current paper.

#### 4.2 Mass Entrainment, Stream Deceleration, and Loss of Kinetic and Thermal Energy

In Fig. 5 we address the cooling and entrainment of background mass onto the stream. In the left hand panel we show the evolution of cold mass in all our simulations. We define “cold” as gas with temperature within a factor 3 of the initial stream temperature,  $T < 3T_s$  (see Table 1 for  $T_s$  values), though our results are not sensitive to this precise choice. In simulations where  $t_{\text{cool, mix}}/t_{\text{shear}} \lesssim 0.1$ , the cold mass begins increasing within less than one stream sound crossing time from the start of the simulation, and grows monotonically as background mass cools and condenses onto the stream. In many cases, the cold mass at  $t \sim 10t_{\text{sc}}$  is  $\sim (3-4)$  times larger than the initial stream mass. In simulations where  $0.1 < t_{\text{cool, mix}}/t_{\text{shear}} < 1$  (M\_2.0\_d100, M\_2.0\_d100\_Hm, M\_1.0\_d100\_LDHR), the cold mass decreases at first, but begins growing after  $\sim (2-3)t_{\text{sc}}$ , and by the end of the simulation at  $10t_{\text{sc}}$  there is more cold gas than at the start of the simulation. However, in simulations where  $1 \lesssim t_{\text{cool, mix}}/t_{\text{shear}}$  (M\_1.0\_d100\_LD, M\_1.0\_d100\_LR), the cold mass decreases with time, since cooling is not fast enough to prevent stream shredding and dilution. This is qualitatively consistent with the NR simulations (dashed lines in the figure), though the cooling does slow down the rate of mass loss and stream expansion, as discussed above. Indeed, the cold mass declines slower for  $t_{\text{cool, mix}}/t_{\text{shear}} \sim 0.97$  (M\_1.0\_d100\_LR) than for  $t_{\text{cool, mix}}/t_{\text{shear}} \sim 2.44$  (M\_1.0\_d100\_LD).

In the right hand panel of Fig. 5 we show the entrainment rate of background gas onto the stream in the simulations, defined as the time derivative of the curves in the left-hand panel. Note that the LD, SR, and NR simulations, where the cold mass is decreasing, are not shown. We compare the measured entrainment rates to the prediction from eq. (16), by scaling them accordingly. When properly scaled, all cases where  $t_{\text{cool, mix}}/t_{\text{shear}} \lesssim 0.1$  coincide to within  $\sim 50\%$  at all times. The asymptotic value is  $\sim 4$ , in agreement with eq. (16). We obtain very similar results by replacing  $t_{\text{cool, 1.5}T_s}$  in eq. (16) with the cooling time evaluated in the temperature range  $(1.2-2)T_s$ . The three simulations where  $0.1 < t_{\text{cool, mix}}/t_{\text{shear}} < 1$  have lower entrainment rates than predicted by eq. (16) by a factor of  $\sim 2-4$ . However, it is possible that these simulations have not yet reached steady-state entrainment, and that this discrepancy will decrease at later times. Additionally, the entrainment rate in the M1.0\_d100\_HR simulation, with  $R_s = 6\text{ kpc}$ , seems not to have converged by  $t = 10t_{\text{sc}}$ . The reasons for this are not entirely clear, and we expect that the entrainment rate will likely

converge at a value  $\lesssim 2$  times larger than the prediction at  $t \gtrsim 10t_{\text{sc}}$ . As the entrainment values are still in reasonable agreement with our model compared to other simulations, we do not currently address this issue further.

As background mass is entrained onto the stream, the stream decelerates due to momentum conservation. In the left hand panel of Fig. 6, we show the stream velocity,  $V_s$ , normalized by its initial value as a function of time normalized by the sound crossing time.  $V_s$  is computed as the average velocity in the  $\hat{z}$  direction, weighted by the stream mass<sup>5</sup> in each cell,  $m_s = \psi m$ , where  $m$  is the total cell mass. It is instructive to compare the magenta, light-grey, and gold lines, which refer to simulations with  $(M_b, \delta) = (1.0, 100)$ , but different stream densities and thus different cooling times. These three simulations have very different deceleration rates, showing that eqs. (7)-(8), which were found to describe stream deceleration in the non-radiative case (M19), are not a valid description for the deceleration of radiatively cooling streams. Note also that the LD simulation (light-grey line) decelerates slower than the corresponding non-radiative case (dashed magenta line), because cooling slows stream expansion in the former despite it being in the regime where  $t_{\text{cool, mix}} > t_{\text{shear}}$ .

Conservation of momentum yields  $V(t) = V_0 m_0 / m(t)$ , where  $m$  represents the cold mass flowing with the stream.<sup>6</sup> As an approximation, we assume

$$m(t) = m_0 + \langle \dot{m} \rangle t = m_0 \left( 1 + \frac{t}{t_{\text{ent}}} \right), \quad (26)$$

where  $\langle \dot{m} \rangle$  is the average entrainment rate and we have introduced the entrainment timescale,

$$t_{\text{ent}} \equiv \frac{m_0}{\langle \dot{m} \rangle} \sim \frac{\delta}{2} \left( \frac{t_{\text{cool, 1.5}T_s}}{t_{\text{sc}}} \right)^{1/4} t_{\text{sc}}, \quad (27)$$

motivated by the right-hand panel of Fig. 5. This results in a predicted velocity as a function of time

$$V_s(t) = \frac{V_{s,0}}{1 + t/t_{\text{ent}}}. \quad (28)$$

In the center panel of Fig. 6, we show the stream velocity as a function of time normalized to  $t_{\text{ent}}$ . All simulations now behave very similarly, and are well described by eq. (28), shown by the thick dot-dashed line. Interestingly, even the LD and SR simulations, where  $t_{\text{cool, mix}} \gtrsim t_{\text{shear}}$  and the cold mass declines with time (Fig. 5), seem to follow this relation.

As discussed in §2.1, since the deceleration is caused by mass entrainment and momentum conservation, the

<sup>5</sup> We weight by stream mass for consistency with P18, M19, and Aung et al. (2019). However, the results are nearly identical when using total mass, since the stream and the background are so well mixed, as evidenced by the uniformity of  $\psi$  seen in Figs. 3 and 4.

<sup>6</sup> For  $M_b \gtrsim 1$ , some momentum is transferred to the hot gas far from the stream. However, this turns out to be very small and does not affect the arguments presented in the text.



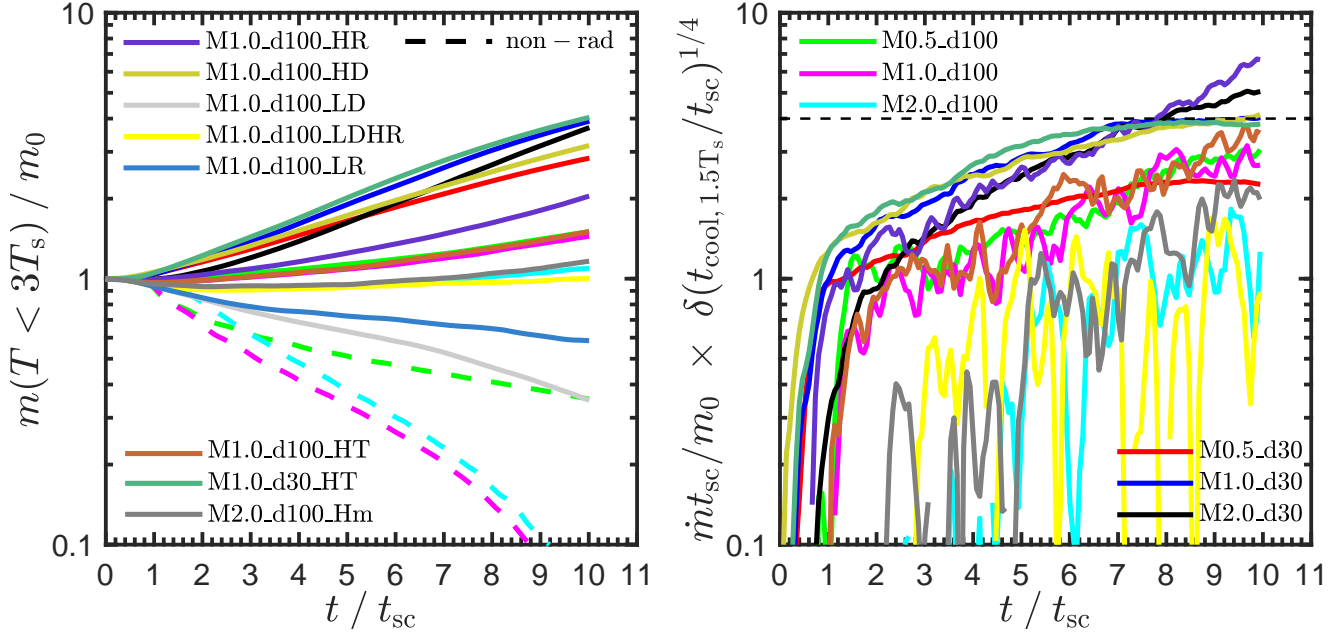


**Figure 5.** Evolution of cold gas mass in the simulations. *Left:* Mass of gas with  $T < 3T_s$  as a function of time, normalized to the initial stream mass. Different colored lines show different simulations (see Table 1), and the dashed lines show the three non-radiative (NR) simulations. In cases where  $t_{cool, mix} > t_{shear}$ , the two LD and three NR simulations, the cold mass decreases with time as the stream expands into the background and is diluted. In all other simulations, where  $t_{cool, mix} < t_{shear}$ , the cold mass increases as background mass cools and condenses onto the stream through the mixing layer. In many cases, the stream mass can increase by a factor of  $\sim (3-4)$  within  $\sim 10t_{sc}$ . *Right:* Entrainment rate of background mass onto the stream, defined as the time derivative of the curves in the left-hand panel, for all cases where  $t_{cool, mix} < t_{shear}$ . These are then scaled according to eq. (16). When properly scaled, the entrainment rates are within  $\lesssim 50\%$  of each other at all times, and the asymptotic value is roughly  $\sim 4$  (horizontal dashed line) as predicted. In cases where  $t_{cool, mix} \gtrsim 0.15t_{shear}$  (M2.0.d100, M2.0.d100-Hm, and M1.0.d100-LDHR), the entrainment rates are slightly lower than predicted.

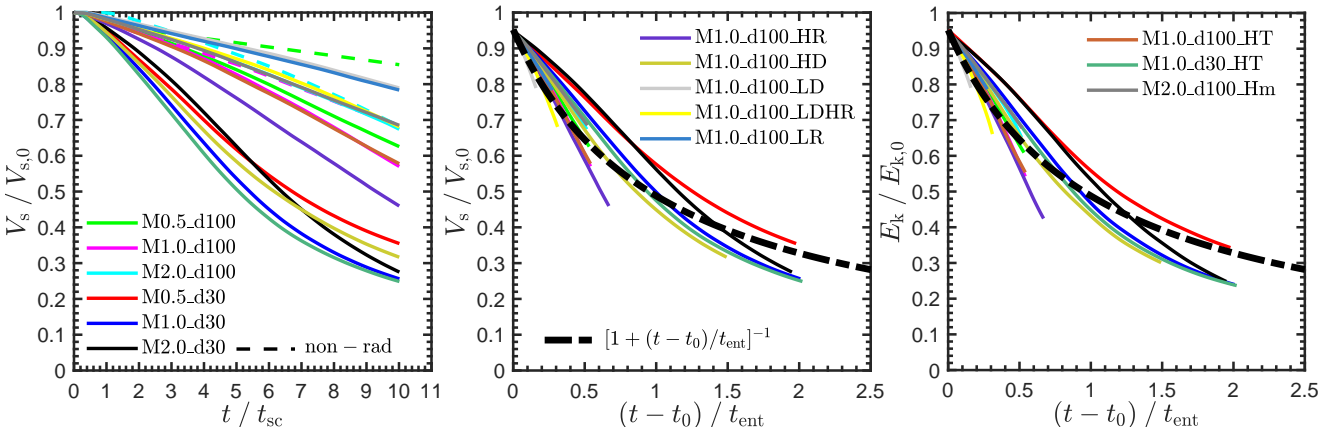


**Figure 6.** Stream deceleration and kinetic energy loss. Line styles and colours are as in Fig. 5. *Left:* Centre of mass velocity of stream fluid (weighted by the passive scalar  $\psi$ ) normalized by its initial value, as a function of time normalized by the stream sound crossing time. By comparing the solid magenta, yellow and grey lines, it is clear that deceleration in radiatively cooling streams does not depend only on  $(M_b, \delta)$ , but on  $t_{cool}$  as well. *Centre:* Same as the left-hand panel, but with the time axis normalized to  $t_{ent}$  (eq. 26), and the zero-point shifted to  $t_0$ , the time at which the velocity reaches 95% of its initial value, in order to avoid focusing on the initial transient before a steady-state is reached. The thick dot-dashed curve shows the predicted deceleration rate (eq. 28), which is found to be a good match to all radiative simulations. *Right:* Total kinetic energy associated with laminar flow of both stream and background fluid, normalized by its initial value, as a function of time normalized by  $t_{ent}$ . The kinetic energy loss is well described by eq. (29), marked by the thick dot-dashed line.

kinetic energy associated with the bulk laminar flow declines as  $E_k(t)/E_{k,0} = V(t)/V_0$ , yielding

$$E_k(t) = \frac{E_{k,0}}{1 + t/t_{\text{ent}}}. \quad (29)$$

In the right-hand panel of Fig. 6, we show the total kinetic energy associated with the laminar flow of both stream and background fluid as a function of time normalized to  $t_{\text{ent}}$ . To compute the kinetic energy, we first compute the mass-weighted mean velocity in the  $\hat{z}$  direction at each radius  $r$ ,

$$\tilde{v}_z(r) \equiv \overline{\rho v_z}(r) / \bar{\rho}(r), \quad (30)$$

where  $\bar{\rho}(r)$  and  $\overline{\rho v_z}(r)$  are obtained analogously to eq. (23). We then compute the kinetic energy associated with this laminar flow, by integrating  $0.5\rho\tilde{v}_z^2$  over the full simulation volume. As expected, eq. (29) (thick dot-dashed line) is a good match to the simulation data.

In addition to the stream losing kinetic energy, the background gas entrained by the stream loses thermal energy, and we wish to examine which dominates the overall energy loss. The rate of thermal energy loss is

$$\dot{E}_{\text{th,b}} = \dot{m}(e_b - e_s) \simeq \dot{m}e_b = \frac{\dot{m}c_b^2}{\gamma(\gamma - 1)} = \frac{9m_0c_b^2}{10t_{\text{ent}}}, \quad (31)$$

where  $e_b = P/[(\gamma - 1)\rho_b]$  is the thermal energy per unit mass of the background fluid which is larger than that in the cold component by a factor  $\delta \gg 1$ ,  $\gamma = 5/3$  is the adiabatic index of the gas, and  $c_b^2 = \gamma P/\rho_b$  is the adiabatic sound speed in the background. In the final equation we have used eq. (26) to approximate  $\dot{m}$ . The total thermal energy lost by time  $t$  is thus

$$\Delta E_{\text{th,b}} = \frac{9m_0c_b^2t}{10t_{\text{ent}}}. \quad (32)$$

Inserting  $E_{k,0} = 0.5m_0V_0^2 = 0.5m_0M_b^2c_b^2$  into eq. (29), we obtain the total kinetic energy lost by time  $t$ ,

$$\Delta E_k = \frac{m_0M_b^2c_b^2}{2} \frac{t/t_{\text{ent}}}{1 + t/t_{\text{ent}}}. \quad (33)$$

We thus obtain the ratio of kinetic to thermal energy loss as a function of time,

$$\frac{\Delta E_k}{\Delta E_{\text{th,b}}} \sim \frac{5M_b^2}{9(1 + t/t_{\text{ent}})}. \quad (34)$$

Figure 7 shows this ratio normalized by  $M_b^2$  as a function of time normalized by  $t_{\text{ent}}$ .  $E_{\text{th,b}}$  is computed in the simulations as the integral of  $\rho_b e_b = (1 - \psi)\rho e_b$  over the full simulation volume. Eq. (34) is a good approximation to all simulations, especially at times  $t \gtrsim 0.5t_{\text{ent}}$ . In particular, this means that most of the energy radiated away is the thermal energy of the background gas, rather than the stream kinetic energy.

### 4.3 Turbulence, Heating, and Mixing

Prior to being radiated away, some fraction of the energy lost from the system as described above will be converted into turbulent kinetic energy and thermal energy in the stream. In this subsection we estimate

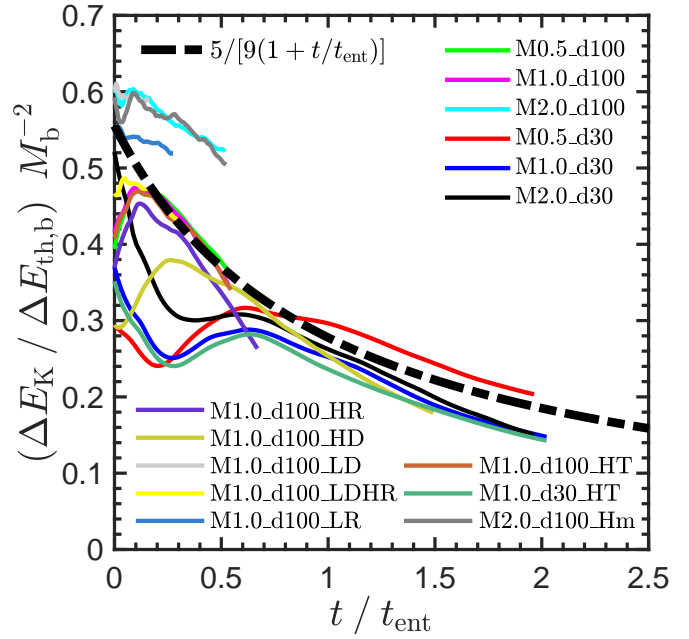


**Figure 7.** Ratio of kinetic to thermal energy loss in the simulations. We show this ratio, normalized by  $M_b^2$ , as a function of time normalized by  $t_{\text{ent}}$ . The thick dot-dashed line shows eq. (34), which is a good match to all simulations at  $t \gtrsim 0.5t_{\text{ent}}$ .

the fraction of the energy budget in each of these components over long timescales. We also examine the density and temperature distributions in the stream and the mixing of stream and background material.

#### 4.3.1 Turbulent Energy and Mach Number

We evaluate the magnitude of turbulence in Fig. 8. In the left-hand panel, we show the ratio of turbulent velocity within the mixing zone,  $\sigma_{\text{turb}}$ , to the initial sound speed in the stream,  $c_s$ . As we show below, the mean stream temperature does not vary much, so this ratio is roughly the turbulent Mach number within the mixing zone.  $\sigma_{\text{turb}}$  is measured in the simulations as

$$\sigma_{\text{turb}}^2 = \frac{\int_{R_s-h_s}^{R_s+h_b} \bar{\rho}(r) [(v_z - \tilde{v}_z)^2 + v_x^2 + v_y^2] r \, dr}{\int_{R_s-h_s}^{R_s+h_b} \bar{\rho} r \, dr}. \quad (35)$$

Note that  $h_s = R_s$  after  $\sim (1 - 3)t_{\text{sc}}$  in all simulations with  $t_{\text{cool,mix}} < t_{\text{shear}}$ . The turbulence generated by the instability is subsonic, with turbulent Mach numbers in the range  $\sim (0.1 - 0.5)$ , or  $\sigma_{\text{turb}} \sim (2 - 10) \text{ km s}^{-1}$ . This is of order the velocity of material flowing through the mixing layer (eq. 15), and is less than the turbulent velocities in the non-radiative case (M19).

In the right-hand panel of Fig. 8 we show the turbulent velocity normalized by  $\delta^{-1/2} V_{s,0}$ . This reduces the scatter between simulations significantly, and we find  $\sigma_{\text{turb}} \sim 0.2 \delta^{-1/2} V_{s,0}$ . This shows that  $\rho_s \sigma_{\text{turb}}^2 \propto \rho_b V_{s,0}^2$ , which in the rest frame of the stream implies that the turbulent energy induced in the stream is proportional to the kinetic energy of the shearing motion. For  $\delta \sim (30 - 100)$ , and for a total mass within



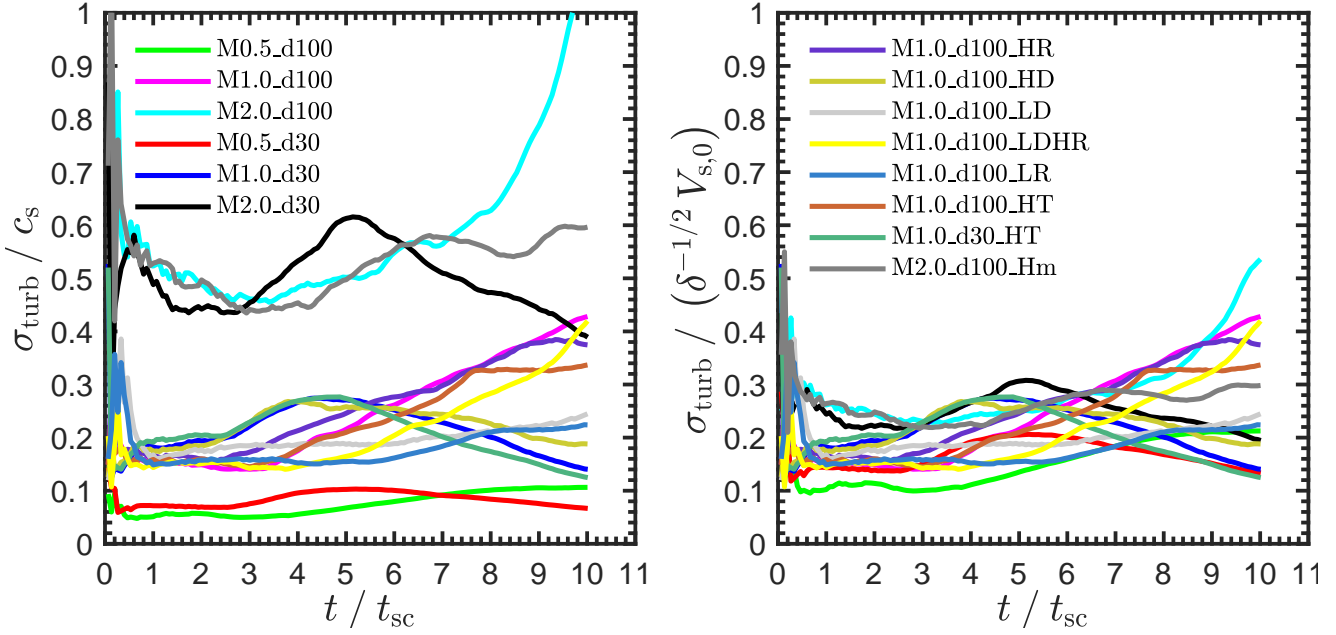


**Figure 8.** Turbulence in the mixing zone as a function of time. *Left:* The turbulent velocity normalized by the initial stream sound speed. The instability drives subsonic turbulence within the stream, with turbulent Mach numbers in the range  $\sim (0.1 - 0.5)$ . *Right:* The turbulent velocity normalized by  $\delta^{-1/2} V_{s,0}$ . In all our simulations,  $\sigma_{\text{turb}} \sim 0.2 \delta^{-1/2} V_{s,0}$ .

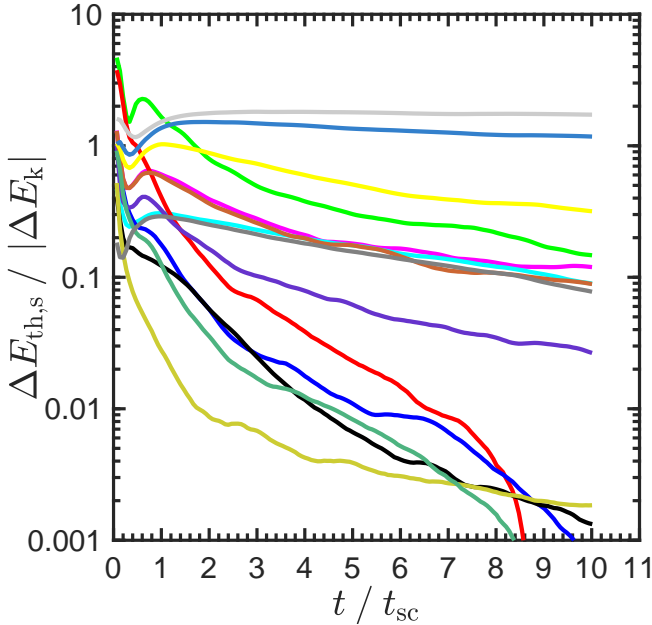


**Figure 9.** Thermal energy increase in the stream from time 0 to  $t$ , normalized by the laminar kinetic energy lost during this time. This ratio decreases with time and with  $t_{\text{cool}, \text{mix}} / t_{\text{shear}}$  (Table 1), is rarely larger than 10%, and is often less than 1%. The legend is omitted for clarity, but is identical to previous figures.

the mixing layer  $\sim (1 - 4)$  times the initial stream mass (Fig. 5), the turbulent kinetic energy is  $\sim (0.5 - 5) \times 10^{-3}$  times the initial kinetic energy of the stream. This is completely negligible compared to the lost laminar kinetic energy (Fig. 6) or background thermal energy (Fig. 9).

#### 4.3.2 Heating of the Stream

In Fig. 9 we show the increase in the thermal energy of the stream fluid from time 0 to time  $t$ , normalized by the laminar kinetic energy lost during this time interval.<sup>7</sup>  $E_{\text{th},s}$  is computed by integrating  $\rho_s e_s = \psi p e_s$  over the simulation volume. The fraction of lost kinetic energy that is converted to thermal energy in the stream decreases with time and with  $t_{\text{cool}, \text{mix}} / t_{\text{shear}}$  (see Table 1). The increase in  $E_{\text{th},s}$  is due both to turbulent decay and to mixing with hot background fluid, which can occur at lower densities farther from the stream axis as the ratio  $t_{\text{cool}, \text{mix}} / t_{\text{shear}}$  increases (Fig. 4). For the M1.0\_d100\_LD and M1.0\_d100\_LR simulations, where  $t_{\text{cool}, \text{mix}} > t_{\text{shear}}$ , the increase in thermal energy of stream fluid compensates for roughly all the lost kinetic energy. For the other cases, the fraction of lost kinetic energy maintained as thermal energy decreases with time, saturating at  $\sim 10\%$  for cases where  $t_{\text{cool}, \text{mix}} \sim 0.1 t_{\text{shear}}$ , and decreasing to  $< 1\%$  for cases where  $t_{\text{cool}, \text{mix}} \lesssim 0.01 t_{\text{shear}}$ .

#### 4.3.3 Temperature and Density Distribution in the Stream

In Fig. 10 we examine the temperature (top panels) and density (bottom panels) distributions of stream gas at  $t = 5 t_{\text{sc}}$  for all simulations. In the top-left-hand panel we show the radial temperature profiles, weighted by total mass in each radial bin. The profiles look qualitatively similar at all times  $t \gtrsim t_{\text{sc}}$ . The transition from  $T_s$  to  $T_b$

<sup>7</sup> As with  $E_{\text{turb}}$ , we are not claiming that the source for the increase in  $E_{\text{th},s}$  is exclusively  $\Delta E_k$  as opposed to  $\Delta E_{\text{th},b}$ , but rather only using  $\Delta E_k$  as a means for quantifying  $\Delta E_{\text{th},s}$ .

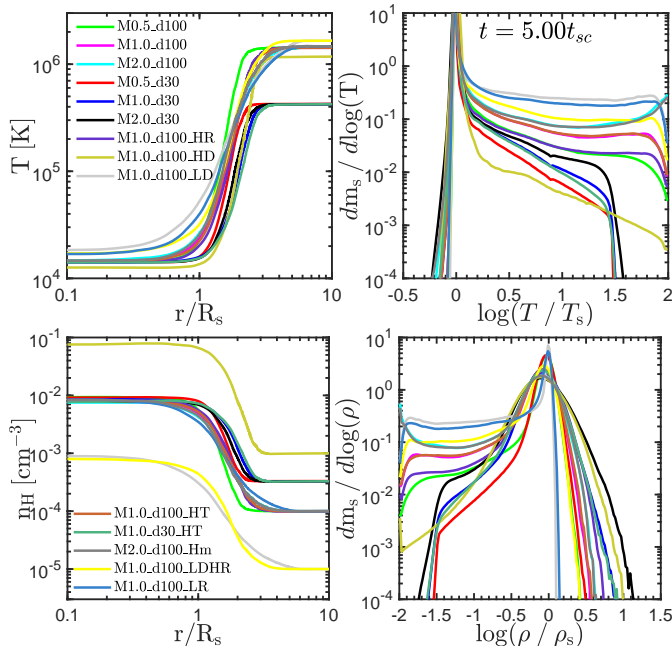


**Figure 10.** Temperature (*top panels*) and density (*bottom panels*) distributions in the stream at  $t = 5t_{sc}$ . *Left panels:* Radial temperature and Hydrogen number density profiles as a function of  $r/R_s$ . All profiles appear qualitatively similar at all times  $t > t_{sc}$ . The transition between the stream and background values begins at  $r \lesssim R_s$ , while its outer radius increases with time. *Right panels:* Temperature and density PDFs weighted by stream-mass,  $m_s = \psi m$ . Temperatures and densities have been normalized by the initial stream values,  $T_s$  and  $\rho_s$ , respectively. The PDFs at all times  $t \gtrsim t_{sc}$  are very similar. The temperature PDFs are sharply peaked at  $T_s$ , with very little mass at  $T < T_s$  and a distribution towards higher  $T$  which increases with the ratio  $t_{cool, mix}/t_{shear}$ . The density PDFs tend to peak at densities  $\lesssim 0.1$  dex lower than  $\rho_s$ , and resemble a log-normal distribution around the peak. Large overdensities are apparent in all simulations with  $t_{cool, mix} < t_{shear}$ , reaching up to a factor of  $\sim 10$  in the most rapidly cooling simulations.

occurs in the radial range  $0.8 \lesssim (r/R_s) \lesssim 2$ , though the radius where  $T$  reaches  $T_b$  increases with time. In the top-right-hand panel we show the temperature PDFs weighted by stream-mass,  $m_s = \psi m$ . The PDFs are very similar at all times  $t > t_{sc}$ . They are sharply peaked near the initial stream temperature,  $T_s$ , with very little stream mass at lower temperatures. The lowest temperatures reached in the simulations are  $\gtrsim 0.6T_s$ . The width of the distribution towards higher temperatures increases with  $t_{cool, mix}/t_{shear}$ , though the half-width-at-half-maximum (HWHM) is  $< 0.05$  dex in all cases. The kinks evident in the black, blue, and red curves correspond to  $T_{max}$  (Table 1).

In the bottom-left-hand panel we show the radial profiles of the Hydrogen number density,  $n_H$ . Similar to the temperature profiles, these are qualitatively similar at all times  $t > t_{sc}$ . The transition from  $n_{H,s}$  to  $n_{H,b}$  occurs over a similar region to the temperature transition, with its width similarly increasing with time. In the bottom-right-hand panel, we show the PDFs of density normalized by the initial stream density,  $\rho_s$ ,

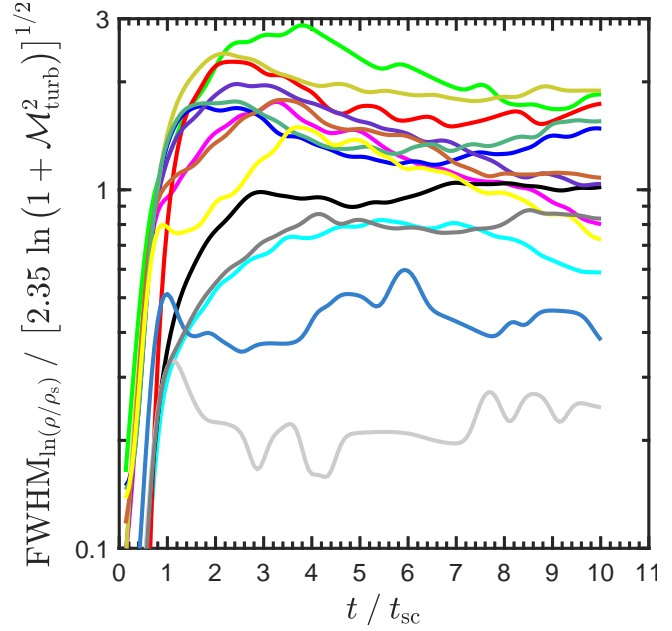


**Figure 11.** FWHM of the density PDFs normalized by the expected value given the turbulent Mach number. Most simulations lie close to unity at all times, implying that the density PDFs are generated by isothermal turbulence. The legend is omitted for clarity, but is identical to previous figures.

and weighted by stream mass. The distribution of gas with  $\rho/\rho_s > 0.1$  is extremely similar when weighting by total mass,  $m$ , rather than stream mass,  $\psi m$ . The time variation of the PDFs at  $t > t_{sc}$  is extremely small. Unlike the narrowness of the temperature PDFs towards low temperatures, the density PDFs are roughly log-normal near their peaks, with overdensities as large as 10 seen in the most rapidly cooling runs. The width of the distribution towards low densities increases with the ratio  $t_{cool, mix}/t_{shear}$ . The difference between the shapes of the density and temperature PDFs indicates that pressure equilibrium is not maintained, or that the turbulent pressure is not negligible.

A log-normal density PDF is expected for isothermal turbulence (e.g. Vazquez-Semadeni 1994; Padoan, Nordlund & Jones 1997; Scalo et al. 1998; Federrath, Klessen & Schmidt 2008; Price, Federrath & Brunt 2011; Hopkins, Quataert & Murray 2012; Konstandin et al. 2012). The width of the distribution is a function of the turbulent Mach number,

$$\sigma_{\ln(\rho)} \simeq [\ln(1 + b_{turb}^2 \mathcal{M}_{turb}^2)]^{1/2}, \quad (36)$$

where  $b_{turb}$  depends on the ratio of compressive to solenoidal forcing driving the turbulence, such that  $b_{turb} = 1, 1/3$ , or  $2/3$  for purely compressive, purely solenoidal, or an equal mixture of compressive and solenoidal forcing, respectively (Federrath, Klessen & Schmidt 2008). While this relation was derived for supersonic turbulence, it is also a good fit for subsonic turbulence, provided the forcing is largely compressive (Konstandin et al. 2012). Precisely fitting the density PDFs is beyond the scope

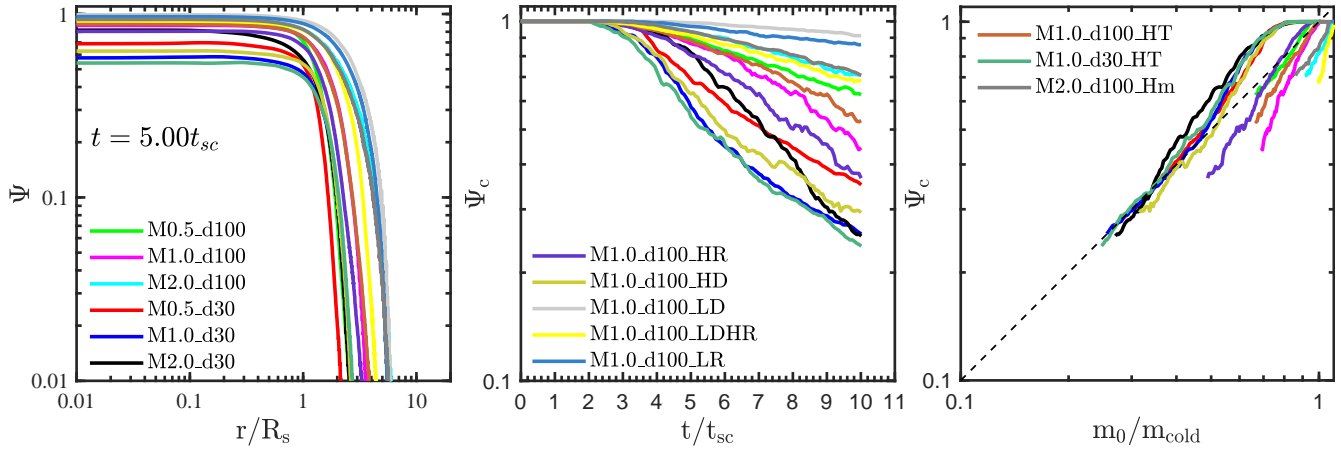


**Figure 12.** Mixing of entrained background material within the stream. *Left:* Radial profiles of the passive scalar  $\psi$  at  $t = 5t_{sc}$ . These are extremely flat within  $R_s$ , suggesting efficient mixing within the stream. *Centre:* The central value of the passive scalar,  $\psi_c = \psi(r = 0)$ , as a function of time. In all cases where  $t_{cool, mix} < t_{shear}$ ,  $\psi_c$  begins declining at  $t \sim (2 - 3)t_{sc}$ , and reaches  $\sim (0.25 - 0.7)$  by  $10t_{sc}$ . *Right:* Here we compare  $\psi_c$  to the ratio of initial stream mass to the total mass of cold gas (see Fig. 5). The simulations lie close to the one-to-one relation (thin dashed line), suggesting that the entrained background material is efficiently mixed within the stream.

of this paper<sup>8</sup>, as is validating via a power spectrum analysis whether the turbulence in our simulations is fully developed. Nonetheless, we test whether eq. (36) is a reasonable description of the simulation data by evaluating the full-width-at-half-maximum (FWHM) of the distributions at each timestep, and using the relation for a log-normal distribution,  $\sigma = \text{FWHM} [8\ln(2)]^{-1/2} \simeq \text{FWHM}/2.35$ . When evaluating the FWHM, we use the natural logarithm,  $\ln$ , rather than the 10-base log shown on the  $x$  axis of the bottom-right-hand panel of Fig. 10,  $\ln(\rho) = \log(\rho)/\log(e) \simeq 2.30 \log(\rho)$ . We compare this to eq. (36) in Fig. 11. We assume  $b = 1$ , corresponding to fully compressive forcing, valid if the turbulence is driven primarily by background gas condensing radially onto the stream, rather than by the shear flow. We use the turbulent Mach numbers presented in the left-hand panel of Fig. 8, i.e. using the initial sound speed of the stream. Although the PDFs appear systematically wider than predicted by eq. (36), for most simulations the discrepancy is less than  $\sim 50\%$  at  $t > (1 - 2)t_{sc}$ . This suggests that the density distribution is indeed generated by near-isothermal turbulence with compressive forcing. The simulations which deviate the most from this relation, and which seem to have too narrow a PDF compared to eq. (36), are those with  $t_{cool, mix}/t_{shear} \gtrsim 1$ , M1.0\_d100\_LD and M1.0\_d100\_LR. These simulations deviate the most from isothermality as evidenced by the temperature PDFs in Fig. 10. The larger stream temperature implies that the effective Mach number is lower than assumed in Fig. 11, which may help bring these curves in better agreement with the prediction.

<sup>8</sup> In particular, we do not differentiate between a log-normal and a skewed log-normal distribution, see Vossberg, Cantalupo & Pezzulli (2019).

#### 4.3.4 Mixing in the Stream

Figures 3 and 4 suggest that when  $t_{cool, mix} < t_{shear}$ , the turbulence leads to very efficient mixing of the background fluid within the stream. We examine this more quantitatively in Fig. 12. In the left-hand panel we show radial profiles of the passive scalar,  $\psi$ , at  $t = 5t_{sc}$ . The profiles are qualitatively similar at all times  $t > t_{sc}$ , and are all remarkably constant within  $R_s$ , suggesting efficient mixing within the stream. In the centre panel we show  $\psi_c = \psi(r = 0)$  as a function of time. For the LD and LR simulations, where  $t_{cool, mix} \gtrsim t_{shear}$ , this declines by  $\sim 10\%$  after  $10t_{sc}$ , consistent with the visual impression in Fig. 4. For all other cases, the central value of  $\psi$  begins declining at  $t \sim (2 - 3)t_{sc}$ , and is  $\sim (0.25 - 0.70)$  at  $t \sim 10t_{sc}$ , suggesting that a significant amount of background material has been deposited near the central axis of the stream. In the right-hand panel we compare  $\psi_c$  to the ratio of initial stream mass to the current mass of cold gas (Fig. 5). If the entrained material were perfectly homogeneously mixed, these two quantities would be equal. While not perfectly equal, they do not lie far from the one-to-one relation, implying that turbulence efficiently mixes the entrained background material within the stream.

#### 4.4 Cooling Emissivity

In §4.2 and §4.3, we quantified the kinetic energy in both laminar flow and turbulent motions, and the thermal energy in both the stream and the background fluids, addressing the transfer of energy between these channels and the loss of energy from the system. We now wish to quantify the cooling emission in our simulations and to compare this to the energy loss associated with the instability.

In the left-hand panel of Fig. 13, we show the net energy dissipation rate in our simulations. This is computed by directly measuring the total kinetic

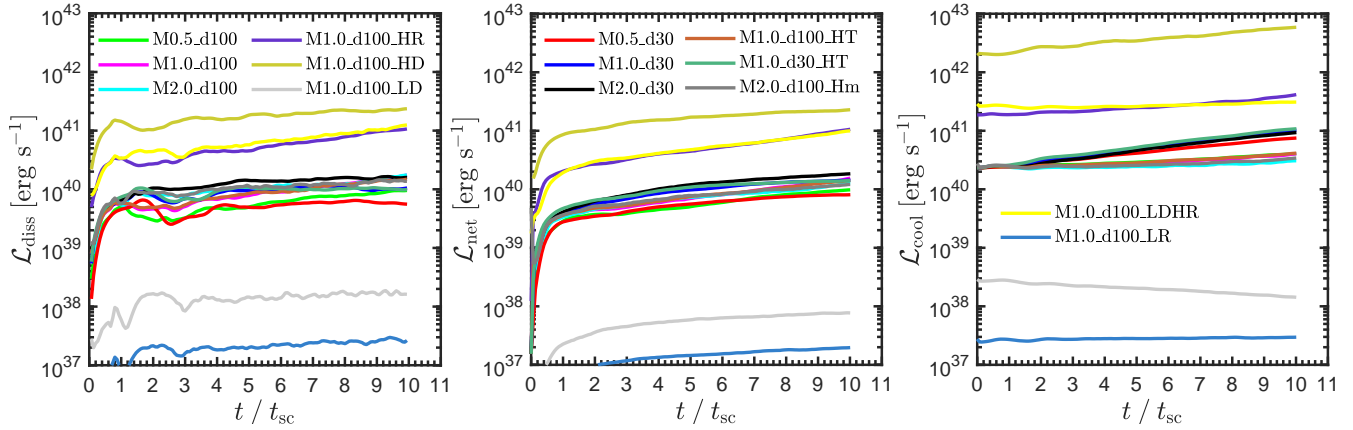


**Figure 13.** Energy dissipation and cooling radiation in the simulations. *Left:* The net energy dissipation rate measured directly from the simulation, accounting for total kinetic energy and thermal enthalpy as well as energy advected across the simulation boundary. *Centre:* Net radiative cooling computed in the simulations at each timestep, after subtracting the radiative heating due to the UV background. This matches the measured energy dissipation remarkably well, and obeys the scaling relations predicted in the text, showing that the dissipation processes described in the previous sections indeed lead to cooling at the predicted rates. *Right:* Total cooling computed in the simulations, without subtracting the radiative heating by the UV background. The cooling induced by the UV background dominates over that induced by the instability, accounting for  $\sim (95, 80, 50)\%$  of the total radiation for stream densities of  $n_{H,s} \sim (0.1, 0.01, 10^{-3}) \text{ cm}^{-3}$  respectively. This contribution will likely be reduced when self-shielding of dense gas is included in the models.

(laminar plus turbulent) and thermal (stream plus background) energy in the simulation volume at each output, while also accounting for energy flux through the simulation boundary (negligible compared to other sources of energy loss). We then compute the energy dissipation rate between two adjacent snapshots. When doing this, we multiply the thermal energy loss by  $(5/3)$ , as expected for an isobaric cooling flow due to the PdV work on the cooling gas compensating for some of the radiated energy (Fabian 1994, G20). In other words, it is the difference in the enthalpy of the gas between two timesteps which is radiated, rather than the internal energy. This was found to be a good description of the emissivity in G20, and we also find it to accurately describe our simulations, as shown below. This is because the background pressure far from the stream remains roughly constant throughout the simulation, and acts as a pressure bath confining the cooling flow of entrained mass onto the stream.

In the centre panel of Fig. 13 we show the net cooling rate in our simulations, computed directly from the **RAMSES** cooling modules after subtracting the heating from the UV background. In this way, we focus only on excess cooling beyond what is needed to maintain thermal equilibrium with the UVB. Recall that we shut off cooling for gas with  $T > T_{\text{max}}$ . These agree remarkably well with the dissipation rates shown in the left-hand panel, showing that the energy loss induced by the instability is emitted as cooling radiation. In Fig. 14 we show the distribution of this radiation as a function of temperature at  $t = 5t_{\text{sc}}$ , but note that the distributions are extremely similar at all  $t > t_{\text{sc}}$ . In all cases, the emission peaks at  $T \sim (1.5 - 2) \times 10^4 \text{ K}$ , and  $\sim 50\%$  of the emission originates from gas with  $T < 5 \times 10^4 \text{ K}$  within the turbulent mixing zone near the stream-background interface. The emission is thus expected to be dominated by Ly $\alpha$

(Goerdt et al. 2010). Note that the emission from gas with  $T$  greater than the fiducial  $T_{\text{max}} \sim 10T_s$  (Table 1) is smaller than gas with  $T \lesssim 3 \times 10^4$  by a factor of  $\sim (10 - 100)$ . This explains why increasing  $T_{\text{max}}$  by a factor of 4 in the two HT runs did not change any of our results (see also G20).

At late times, the energy loss is dominated by the thermal energy of background gas, given by eq. (31). Together with eq. (27), this implies that

$$\begin{aligned} \mathcal{L}_{\text{diss}} &\propto m_0 c_b^2 t_{\text{ent}}^{-1} \propto n_s R_s^2 L c_b^2 \delta^{-1} t_{\text{cool}}^{-1/4} t_{\text{sc}}^{-3/4} \\ &\propto n_s^{5/4} R_s^{5/4} L c_s^{11/4}, \end{aligned} \quad (37)$$

where  $L$  is the stream length, and we have used the fact that  $t_{\text{cool}} \propto n^{-1}$ , and that  $\delta^{-1} c_b^2 = c_s^2$ . All our simulations have comparable stream temperatures and sound speeds, while the stream length is  $L = 32R_s$ . We thus obtain  $\mathcal{L}_{\text{diss}} \propto n_s^{5/4} R_s^{9/4}$ . This explains why, in Fig. 13, all simulations with  $n_{H,s} = 0.01 \text{ cm}^{-3}$  and  $R_s = 3 \text{ kpc}$  have roughly the same luminosity, while the luminosity in the HR simulation with  $R_s = 6 \text{ kpc}$  (purple line) is a factor of  $\sim 5$  larger, and that in the HD simulation with  $n_{H,s} = 0.1 \text{ cm}^{-3}$  (yellow line) is a factor of  $\sim 20$  larger. The luminosity in the LD, LR, and LDHR simulations are lower than expected from this scaling. These have the largest ratios of  $t_{\text{cool, mix}}/t_{\text{shear}}$  among our simulations (Table 1), so the entrainment of background gas onto the stream is suppressed and the scaling relations derived above do not strictly apply. In a companion paper (Mandelker et al. 2020), we use these results to estimate the total luminosity emitted by a cosmological cold stream in a dark matter halo potential as a result of these dissipation processes.

In the right-hand panel of Fig. 13, we show the total cooling luminosity in the simulations, computed from the **RAMSES** cooling modules without subtracting



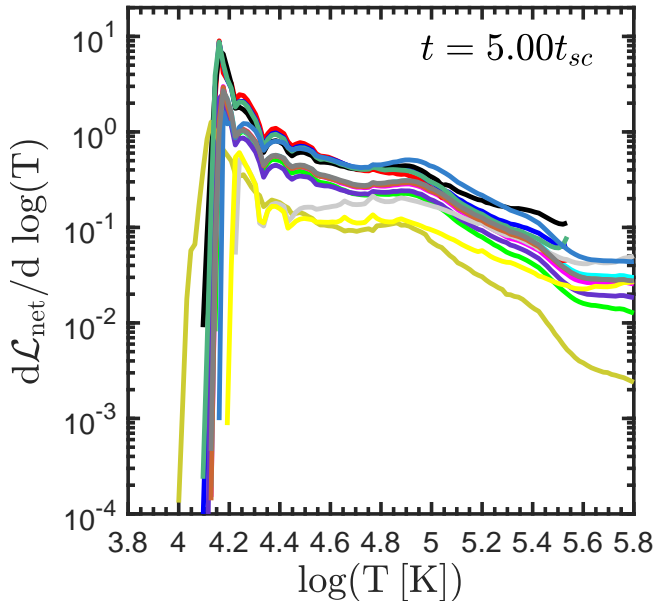


**Figure 14.** PDF of net radiative cooling computed in the simulations, as a function of gas temperature, at  $t = 5t_{sc}$ . Each curve is normalized to an integral of unity, while the total luminosity can be read from the centre panel of Fig. 13. In all cases, the radiation is dominated by gas with  $T \sim (2-3) \times 10^4$  K. The legend is omitted for clarity, but is identical to previous figures.

the radiative heating by the UVB. Comparing this to the centre panel, it is clear that without self-shielding the cooling induced by the UVB dominates over the dissipation processes described above. The latter comprise  $\sim 50\%$ ,  $20\%$ , and  $5\%$  of the total emission for  $n_{H,s} \sim 10^{-3}$ ,  $10^{-2}$ , and  $10^{-1} \text{ cm}^{-3}$ , respectively. The increased emission due to UV heating is primarily from gas near the thermal equilibrium temperature with  $T \sim T_s$  in the stream interior. The large overdensities in the cold gas (bottom-right-hand panel of Fig. 10) yield particularly large emissivity in this regime, especially in the HD simulation. Metal line cooling at  $T < 10^4$  has a negligible contribution to the total emissivity. We defer a more detailed exploration of the resulting spectrum, and the relative importance of UV heating versus KHI induced dissipation, to future work which will include self-shielding (see §5).

## 5 CAVEATS AND ADDITIONAL PHYSICS

While our analysis has been thorough in terms of the effect of radiative cooling on stream evolution, there are many physical processes relevant for astrophysical cold streams which are still unaccounted for in our models. Some of these have been addressed by other authors, though not in combination with radiative cooling. In this section we address these additional processes, and speculate how they may influence our results.

Before addressing additional physics, we note that Vossberg, Cantalupo & Pezzulli (2019) used 2d purely hydrodynamic simulations to study the amplitude of

KHI-induced density fluctuations within cold streams. They found the resulting density fluctuations both short lived and small compared to those inferred from observations of the CGM of galaxies expected to host cold streams, and concluded that additional physical processes, such as cooling or gravity, were necessary to achieve such large density fluctuations. As we have shown, radiative cooling enhances the density fluctuations within streams, and prolongs their lifetime since the stream density is not diluted by the KHI (Figs. 2, 4, and 10). However, these fluctuations are still small compared to those inferred from observations. In some cases, the lognormal dispersion is inferred to be as large as  $\sigma_{\ln(\rho)} \sim 2.5$  (Cantalupo et al. 2019). This implies  $\text{FWHM}_{\log(\rho)} \sim 2.6$ , much larger than seen in our simulations (Fig. 10, bottom-right). It thus seems that if KHI in cold streams is to explain the large density fluctuations observed, additional physical processes beyond radiative cooling are required.

One such process may be self-shielding. The cold streams are expected to be largely self-shielded from the UV background, as discussed in Faucher-Giguère et al. (2010) and Goerdt et al. (2010), who studied the emission properties of cold streams using cosmological simulations. These two studies disagreed on the density above which self-shielding becomes important, with estimates ranging from  $n_H \sim (0.01 - 0.1) \text{ cm}^{-3}$ , causing their estimates for the  $\text{Ly}\alpha$  emissivity in cold streams to vary by more than an order of magnitude. As we have shown, in the limit of no self-shielding the cooling radiation induced by the UV background can be much larger than that induced by the instability (Fig. 13). Furthermore, as self-shielding affects the thermal and ionization state of the gas, it must be accounted for in order to properly estimate the fraction of radiation emitted in  $\text{Ly}\alpha$ , even only considering radiation induced by the instability. Finally, self-shielding is likely to widen the density distribution within the streams. The overdensities of a factor  $\sim (3 - 10)$  produced in our current simulations may be able to cool below  $10^4$  K, especially given the efficient mixing of background metals in the stream (Fig. 12), thereby reaching even higher densities. We will include self-shielding in our models in an upcoming paper.

Another important process affecting the density distribution and morphology of streams is self-gravity. The importance of self-gravity in streams can be assessed by comparing the mass per unit length of the stream,  $\lambda = \pi R_s^2 \rho_s$ , to the maximal mass per unit length possible for an isothermal stream in hydrostatic equilibrium (Ostriker 1964),

$$\lambda_{\text{max}} = 2c_s^2/G \simeq 10^5 M_\odot \text{ pc}^{-1} T_4 \mu_{s,0.6}^{-1}, \quad (38)$$

where  $G$  is Newton’s gravitational constant, and  $\mu_{s,0.6} = \mu_s/0.6$ , with  $\mu_s$  the mean molecular weight in the stream. If the stream is strongly self-shielded and predominantly neutral,  $\mu_{s,0.6} \sim 2$ . The mass per unit length of the stream can be constrained via the mass accretion rate through the stream (P18; Mandelker et al. 2018, 2020),  $\dot{M}_s \sim \pi R_s^2 \rho_s V_s \sim f_s f_b \dot{M}_v$ , where  $V_s = \eta V_v$  is the stream velocity which is of

order the virial velocity (i.e.  $\eta \sim 1$ ),  $\dot{M}_v$  is the total mass accretion rate through the virial radius,  $f_b$  is the Universal baryon fraction, and  $f_s$  is the fraction of the total accretion along a given stream. Note that we have assumed here that the baryonic accretion is predominantly gas, which is a reasonable assumption at high redshift. Cosmological simulations suggest  $f_s \sim (0.2 - 0.5)$  with a typical value of  $f_s = 1/3$  (Danovich et al. 2012). In the Einstein de Sitter (EdS) regime (valid at  $z > 1$ ), the accretion onto the virial radius is well approximated by (Dekel et al. 2009, 2013)  $\dot{M}_v \sim 468 M_\odot \text{yr}^{-1} M_{12} (1+z)_3^{5/2}$ , with  $M_{12} = M_v/10^{12} M_\odot$  and  $(1+z)_3 = (1+z)/3$ . The virial velocity is (Dekel et al. 2013)  $V_v \sim 200 \text{ km s}^{-1} M_{12}^{1/3} (1+z)_3^{1/2}$ . Taking all this together, we have

$$\lambda/\lambda_{\text{max}} \simeq 1.2 M_{12}^{2/3} (1+z)_3^2 \tilde{s} \eta^{-1} T_4^{-1} \mu_{s,0.6}, \quad (39)$$

where  $\tilde{s} \sim (0.3 - 3)$  accounts for halo-to-halo variance in the normalization of  $\dot{M}_v$  and  $f_s$ . This implies that for a wide range of stream parameters hydrostatic equilibrium may not be possible. This was discussed by Mandelker et al. (2018), who speculated that this could lead to gravitational collapse and star formation in streams within the CGM, and potentially even to the formation of globular clusters at high redshift. Heating by a UV background yields  $T_4 \gtrsim (1.5 - 2)$  (Table 1) which can help stabilize the stream. However, self-shielding will enhance the instability, by allowing the stream to cool below  $10^4 \text{ K}$ , reducing  $T_4$  and increasing  $\mu_{s,0.6}$  (see also Li et al. 2019).

If  $\lambda < \lambda_{\text{max}}$ , self-gravity can still influence the development of KHI in the streams. This regime was studied by Aung et al. (2019), who found that if  $\lambda$  was smaller than a critical value  $\lambda_{\text{crit}} < \lambda_{\text{max}}$  (which is larger for denser and faster streams), then stream deceleration proceeds very similarly to the non-gravitating case studied in M19, but total stream disruption is slowed by a factor of  $\gtrsim 3$  due to buoyancy forces near the stream core, even for very low values of  $\lambda$ . This allows streams  $\gtrsim 3$  times thinner than the M19 estimate to reach the central galaxy, irrespective of radiative cooling. For  $\lambda_{\text{crit}} < \lambda < \lambda_{\text{max}}$ , the stream was found to fragment into long-lived, dense, pressure-confined clumps. Furthermore, self-gravity will likely enhance the large overdensities we find in our simulations with cooling, and these may trigger local gravitational instabilities, in addition to the global fragmentation discussed in Mandelker et al. (2018) and Aung et al. (2019). We will study the combined effects of cooling and gravity in an upcoming paper (Cornuault et al. in prep.).

Thermal conduction can hinder both hydrodynamic and thermal instabilities, and may be important for the evolution of a multiphase medium (e.g. Armillotta, Fraternali & Marinacci 2016; Armillotta et al. 2017; Li et al. 2019). In particular, this may influence whether the hot gas cools and condenses onto the stream, as in our simulations, or whether the cold stream diffuses and mixes into the background. For a cold cloud embedded in a hot medium, radiative processes dominate over thermal conduction if the cloud

is larger than the Field Length (Begelman & McKee 1990; Armillotta, Fraternali & Marinacci 2016),

$$L_{\text{Field}} = \left( \frac{\kappa_{\text{Sp}} T_h}{n_e^2 \Lambda(T_c)} \right)^{1/2}, \quad (40)$$

where

$$\kappa_{\text{Sp}} \simeq \frac{1.84 \times 10^{-5}}{\ln(\Psi)} T_h^{5/2} \text{ erg s}^{-1} \text{ K}^{-1} \text{ cm}^{-1} \quad (41)$$

is the Spitzer heat conduction coefficient and

$$\ln(\Psi) \simeq 29.7 + \ln \left[ \frac{T_e/10^6 \text{ K}}{\sqrt{n_e/\text{cm}^{-3}}} \right] \quad (42)$$

is the Coulomb logarithm, with  $T_e$  and  $n_e$  the electron temperature and density in the hot phase. For cold streams, using  $T_e \sim 10^6 \text{ K}$  and  $n_e \sim 5 \times 10^{-5} \text{ cm}^{-3}$ , which are typical conditions for the hot CGM gas near  $R_v$  in a  $\sim 10^{12} M_\odot$  halo at  $z \sim 2$ , we obtain  $\ln(\Psi) \sim 35$ . Inserting this and eq. (41) into eq. (40), along with  $T_h = 10^6 \text{ K} \delta_{100} T_4$  with  $\delta_{100} = \delta/100$  and  $T_4 = T_s/10^4 \text{ K}$ , yields

$$L_{\text{Field}} \simeq 0.2 \text{ kpc} \frac{\delta_{100}^{7/4} T_4^{7/4}}{\Lambda_{-23}^{1/2} n_{s,0.01}}, \quad (43)$$

where  $\Lambda_{-23} = \Lambda(T_s)/10^{-23} \text{ erg s}^{-1} \text{ cm}^3$ , normalized to the approximate cooling rate at  $T \sim 1.5 T_s$  in the presence of a  $z = 2$  UV background as we have assumed throughout.  $L_{\text{Field}}$  is thus comparable to  $R_{s,\text{crit}}$  (eq. 17), below which cooling is unimportant irrespective of thermal conduction. Even if  $\Lambda_{-23} \sim 0.1$ , which may be the case if the streams are self-shielded and  $T_s \lesssim 10^4 \text{ K}$ ,  $L_{\text{Field}}$  is still small compared to the radius of a typical stream (eq. 18). We conclude that thermal conduction is unlikely to affect our main conclusions regarding stream evolution in the presence of cooling, though it may influence the late time shattering of the stream into dense cloudlets seen in Fig. 2.

When considering thermal conduction, we must also consider magnetic fields, which can significantly lower the thermal conductivity below the Spitzer value, particularly perpendicular to the shear direction, and reduce the Field length even further. On the other hand, magnetic fields may stabilize the stream against KHI and prevent mixing of the stream and background gas irrespective of thermal conduction. Berlok & Pfrommer (2019b) studied the influence of magnetic fields on the development of KHI in cold streams, while also carefully accounting for the influence of a smooth transition between the stream and the background following Berlok & Pfrommer (2019a). They find that while magnetic fields can enhance the linear growth rates of the instability, they inhibit stream disruption by suppressing the mixing of the stream and background gas. They estimate that magnetic field strengths of  $(0.3 - 0.8) \mu\text{G}$  allow streams to survive for  $\sim (2 - 8)$  times longer than the non-magnetic case. It is interesting that radiative cooling, self-gravity, and magnetic fields all seem to prolong the lifetime of streams when acting alone, though for different reasons. For example,

magnetic fields prevent the mixing of hot and cold gas thus keeping the stream dense and collimated, while it is precisely this mixing which allows radiative cooling to maintain high densities long-lived streams. In future work, we will study the effects of these physical processes acting in unison on the lifetime and morphology of cold streams.

The gravitational potential of the dark matter halo into which the stream are flowing will have three main effects: (1) the streams will be accelerated towards the halo centre which can counteract the KHI induced deceleration, (2) there will be a gradient in density and pressure in both the background gas and the stream gas, and (3) the stream cross section will decrease with halocentric radius due to both the external pressure gradient as well as pure gravitational focusing. In a companion paper (Mandelker et al. 2020) we present a toy model attempting to account for these processes analytically, and to estimate the resulting profile of stream velocity, mass entrainment, and emitted luminosity. In the future, we also plan to study this directly using idealized simulations of streams embedded in an external potential.

Finally, several groups have recently performed cosmological simulations with enhanced refinement in the CGM (Hummels et al. 2018; Peebles et al. 2019; van de Voort et al. 2019). While the galaxies simulated in these works are less massive than those considered here and may not host a hot static halo at  $z \gtrsim 2$ , and the resolution in the CGM is still lower than in our idealized simulations by a factor of a few, we may soon be able to study stream evolution with adequate spatial resolution in fully cosmological simulations. This will allow for self-consistent generation of linear and non-linear perturbations, the interactions of streams with outflows from the central galaxy and with satellite galaxies along the streams, and the complex interaction between multiple streams and the central galaxy in the inner halo, all of which are likely important for the eventual fate of cold streams, and the emission they may produce.

## 6 SUMMARY AND CONCLUSIONS

Massive halos of  $M_v \gtrsim 10^{12} M_\odot$  at redshift  $z \gtrsim 2$  are thought to be fed by cold streams with temperatures  $T_s \gtrsim 10^4$  K. These streams flow along cosmic web filaments and penetrate the hot CGM of these halos, with  $T_h \sim 10^6$  K. The streams have Mach numbers of  $M_b \sim (0.75 - 2.25)$  with respect to the halo sound speed, density contrasts of  $\delta \sim (30 - 300)$  compared to the background density (assuming pressure equilibrium with the halo gas), radii  $R_s \sim (0.03 - 0.30)$  times the halo virial radii, and Hydrogen number densities in the range  $n_{H,s} \sim (0.1 - 5) \times 10^{-2} \text{ cm}^{-3}$ . In order to study the evolution of such streams as they interact with the hot CGM on their way towards the central galaxies, we presented here a detailed analysis of the non-linear stages of Kelvin-Helmholtz Instability (KHI) in the presence of radiative cooling and heating by a

UV background, though neglecting for the time being self-shielding and thermal conduction. This extended our previous work on the purely hydrodynamic case (Mandelker et al. 2016, 2019a; Padnos et al. 2018), and on the self-gravitating case (Aung et al. 2019), though our current models do not account for gravity. Our main results can be summarised as follows:

(i) The key parameter in determining the fate of the streams is the ratio  $t_{\text{cool,mix}}/t_{\text{shear}}$ , where  $t_{\text{cool,mix}}$  is the cooling time in the turbulent mixing layer which forms at the stream-background interface as a result of the instability, and  $t_{\text{shear}}$  is the timescale for the shear layer to grow to the width of the stream in the non-radiative case analysed by Mandelker et al. (2019a). If  $t_{\text{cool,mix}} > t_{\text{shear}}$ , the behaviour is very similar to the non-radiative case, the stream expands and mixes into the background, its density is diluted, and it is eventually disrupted (Fig. 4). If  $t_{\text{cool,mix}} < t_{\text{shear}}$ , on the other hand, KHI does not disrupt the stream. Rather, background gas cools and condenses onto the stream, increasing the cold gas mass by up to a factor of  $\sim 3$  within 10 stream sound crossing times, though for  $0.1t_{\text{shear}} \lesssim t_{\text{cool,mix}} \lesssim t_{\text{shear}}$ , the entrainment rates are a factor of a few lower (Fig. 5). In this regime, the stream remains cold, dense and collimated until very late times, when it may fragment into small cloudlets (Figs. 2-4), either due to thermal instabilities (McCourt et al. 2018) or secondary instabilities following the development of long wavelength perturbations (Mandelker et al. 2019a). Similar behaviour was found for cold clouds accelerating in a hot wind (Gronke & Oh 2018, 2020; Li et al. 2019).

(ii) The condition  $t_{\text{cool,mix}} = t_{\text{shear}}$  can be translated to a critical stream radius,  $R_s = R_{s,\text{crit}}$ , such that  $R_s/R_{s,\text{crit}} = t_{\text{shear}}/t_{\text{cool,mix}}$  (Fig. 1). For realistic cold streams feeding hot halos,  $R_s > R_{s,\text{crit}}$  except for very extreme parameters, and nearly irrespective of the metallicity in the stream (eqs. 17-19). This implies that it is very difficult for such streams to be disrupted by hydrodynamic instabilities in the CGM of massive halos before reaching the central galaxy. Moreover,  $R_{s,\text{crit}}$  is comparable to the Field length assuming Spitzer conductivity (eq. 43), so thermal conduction is unlikely to affect these conclusions.

(iii) The entrained background gas rapidly mixes with the stream gas (Figs. 3, 4, 12). This causes the stream to decelerate and loose bulk kinetic energy as a result of momentum conservation (Fig. 6). However, for  $M_b \lesssim 1$ , the kinetic energy loss is small,  $\lesssim 30\%$ , compared to the thermal energy lost by the background gas as it condenses onto the stream (Fig. 7). For  $M_b \sim 2$ , or for cases where  $t_{\text{cool,mix}} > t_{\text{shear}}$ , the bulk kinetic energy losses become comparable to or can exceed the thermal energy losses.

(iv) In steady state, roughly  $\sim (1 - 10)\%$  of the bulk kinetic energy losses up to that time are maintained as excess thermal energy within the stream (Fig. 9). The remainder is radiated away, together with the thermal enthalpy losses of the background gas. The turbulent velocities in the mixing layer are  $\sigma_{\text{turb}} \sim$



$0.2V_{s,0}\delta^{-1/2}$ , corresponding to turbulent Mach numbers of  $\mathcal{M}_{\text{turb}} \sim (0.1 - 0.5)$  with respect to the cold component (Fig. 8), or velocities of  $\sigma_{\text{turb}} \sim (2 - 10) \text{ km s}^{-1}$ . Such a stream detected in absorption would be dominated by thermal broadening, consistent with a claimed detection of a cold stream in absorption around a massive star-forming galaxy at  $z \sim 2.5$  (Crighton, Hennawi & Prochaska 2013).

(v) The turbulence appears to be driven by primarily compressive forcing, resulting from the radial condensation of background gas onto the stream. This induces a roughly lognormal density distribution in the stream, whose width follows the predicted relation with turbulent Mach number (Figs. 10 - 11; Konstandin et al. 2012). Overdensities of a factor  $\sim (3 - 10)$  are not uncommon in the streams, even at late times, though the distribution is still narrow compared to that inferred from observations (Cantalupo et al. 2019). The temperature distribution, on the other hand, remains sharply peaked around the initial stream temperature, with very little gas at lower temperatures. This is a result of heating from the UV background, and is likely to change once self-shielding of dense gas is accounted for. This is also likely to broaden the density PDF, particularly in conjunction with self-gravity (Aung et al. 2019), possibly bringing the density fluctuations more in line with observations.

(vi) The total cooling emission from our model streams is dominated by UV background heating. This comprises  $\sim (50 - 95\%)$  of the total emission, depending on stream density. However, this will almost certainly change when self-shielding is included in our models. The excess cooling radiation, beyond that induced by the UV background, is in excellent agreement with the net energy dissipation rates predicted by our model (Fig. 13). Roughly half of the emissivity originates from gas with  $T < 5 \times 10^4 \text{ K}$  within the turbulent mixing layer near the stream interface (Fig. 14), despite the fact that most of the energy loss is the thermal energy of the hot background, with  $T \sim 10^6 \text{ K}$ . The emission is thus expected to be dominated by  $\text{Ly}\alpha$ . We present predictions for the total emitted luminosity of cold streams in dark matter halos in a companion paper (Mandelker et al. 2020), though detailed predictions of the emission spectrum await the inclusion of self-shielding in our models.

## ACKNOWLEDGMENTS

We thank the anonymous referee for a constructive and substantive report which helped improve the quality and accuracy of this manuscript. We thank Romain Teyssier for making **RAMSES** publicly available, and for his many helpful suggestions when running the simulations. We thank Thomas Berlok, Andi Burkert, Nicolas Cornuault, Drummond Fielding, Max Gronke, Joseph F. Hennawi, Suoqing Ji, Neal Katz, S. Peng Oh, Christoph Pfrommer, X. Prochaska, Santi Roca-Fabrega, and Chuck Steidel for helpful discussions. The simulations were performed on the Grace cluster at Yale and the magny cluster

at HITS. NM and FCvdB acknowledge support from the Klaus Tschira Foundation through the HITS Yale Program in Astropysics (HYPA). AD is partly supported by the grants NSF AST-1405962, BSF 2014-273, GIF I-1341-303.7/2016, and DIP STE1869/2-1 GE625/17-1. YB acknowledges ISF grant 1059/14. FCvdB received additional support from the National Aeronautics and Space Administration through grant No. 17-ATP17-0028 issued as part of the Astrophysics Theory Program.

## REFERENCES

- Armillaotta L., Fraternali F., Marinacci F., 2016, *MNRAS*, 462, 4157
- Armillaotta L., Fraternali F., Werk J. K., Prochaska J. X., Marinacci F., 2017, *MNRAS*, 470, 114
- Arrigoni Battaia F., Prochaska J. X., Hennawi J. F., Obreja A., Buck T., Cantalupo S., Dutton A. A., Macciò A. V., 2018, *MNRAS*, 473, 3907
- Aung H., Mandelker N., Nagai D., Dekel A., Birnboim Y., 2019, *MNRAS*, 490, 181
- Begelman M. C., Fabian A. C., 1990, *MNRAS*, 244, 26P
- Begelman M. C., McKee C. F., 1990, *ApJ*, 358, 375
- Behroozi P., Wechsler R. H., Hearin A. P., Conroy C., 2019, *MNRAS*, 1134
- Berlok T., Pfrommer C., 2019a, *MNRAS*, 485, 908
- Berlok T., Pfrommer C., 2019b, *arXiv e-prints*, arXiv:1904.02167
- Birnboim Y., Dekel A., 2003, *MNRAS*, 345, 349
- Bodo G., Massaglia S., Rossi P., Trussoni E., Ferrari A., 1993, *Physics of Fluids*, 5, 405
- Borisova E. et al., 2016, *ApJ*, 831, 39
- Bouché N. et al., 2016, *ApJ*, 820, 121
- Bouché N., Murphy M. T., Kacprzak G. G., Péroux C., Contini T., Martin C. L., Dessauges-Zavadsky M., 2013, *Science*, 341, 50
- Cantalupo S., Arrigoni-Battaia F., Prochaska J. X., Hennawi J. F., Madau P., 2014, *Nature*, 506, 63
- Cantalupo S. et al., 2019, *MNRAS*, 483, 5188
- Ceverino D., Dekel A., Bounaud F., 2010, *MNRAS*, 404, 2151
- Chandrasekhar S., 1961, *Hydrodynamic and hydromagnetic stability*
- Codis S., Pichon C., Devriendt J., Slyz A., Pogossyan D., Dubois Y., Sousbie T., 2012, *MNRAS*, 427, 3320
- Corlies L., Peebles M. S., Tumlinson J., O’Shea B. W., Lehner N., Howk J. C., O’Meara J. M., 2018, *arXiv e-prints*
- Crighton N. H. M., Hennawi J. F., Prochaska J. X., 2013, *ApJ*, 776, L18
- Danovich M., Dekel A., Hahn O., Ceverino D., Primack J., 2015, *MNRAS*, 449, 2087
- Danovich M., Dekel A., Hahn O., Teyssier R., 2012, *MNRAS*, 422, 1732
- Dekel A., Birnboim Y., 2006, *MNRAS*, 368, 2
- Dekel A. et al., 2009, *Nature*, 457, 451
- Dekel A., Zolotov A., Tweed D., Cacciato M., Ceverino D., Primack J. R., 2013, *MNRAS*, 435, 999
- Dijkstra M., Loeb A., 2009, *MNRAS*, 400, 1109

- Dimotakis P. E., 1991, Turbulent free shear layer mixing and combustion. Tech. rep.
- Elmegreen D. M., Elmegreen B. G., Ravindranath S., Coe D. A., 2007, *ApJ*, 658, 763
- Fabian A. C., 1994, *ARA&A*, 32, 277
- Faucher-Giguère C.-A., Kereš D., Dijkstra M., Hernquist L., Zaldarriaga M., 2010, *ApJ*, 725, 633
- Faucher-Giguère C.-A., Kereš D., Ma C.-P., 2011, *MNRAS*, 417, 2982
- Federrath C., Klessen R. S., Schmidt W., 2008, *ApJ*, 688, L79
- Förster Schreiber N. M., Genzel R., Bouché N., Cresci G., Davies R., Buschkamp P., Shapiro K., et al., 2009, *ApJ*, 706, 1364
- Förster Schreiber N. M., Genzel R., Lehnert M. D., Bouché N., Verma A., Erb D. K., Shapley A. E., et al., 2006, *ApJ*, 645, 1062
- Fumagalli M. et al., 2017, *MNRAS*, 471, 3686
- Fumagalli M., Prochaska J. X., Kasen D., Dekel A., Ceverino D., Primack J. R., 2011, *MNRAS*, 418, 1796
- Genzel R., Burkert A., Bouché N., Cresci G., Förster Schreiber N. M., Shapley A., Shapiro K., et al., 2008, *ApJ*, 687, 59
- Genzel R., Tacconi L. J., Eisenhauer F., Förster Schreiber N. M., Cimatti A., Daddi E., Bouché N., et al., 2006, *Nature*, 442, 786
- Goerdt T., Ceverino D., 2015, *MNRAS*, 450, 3359
- Goerdt T., Dekel A., Sternberg A., Ceverino D., Teyssier R., Primack J. R., 2010, *MNRAS*, 407, 613
- Goerdt T., Dekel A., Sternberg A., Gnat O., Ceverino D., 2012, *MNRAS*, 424, 2292
- Gronke M., Oh S. P., 2018, *MNRAS*, 480, L111
- Gronke M., Oh S. P., 2020, *MNRAS*, 492, 1970
- Haardt F., Madau P., 1996, *ApJ*, 461, 20
- Hardee P. E., Stone J. M., 1997, *ApJ*, 483, 121
- Harford A. G., Hamilton A. J. S., 2011, *MNRAS*, 416, 2678
- Hopkins P. F., Quataert E., Murray N., 2012, *MNRAS*, 421, 3488
- Hummels C. B. et al., 2018, *arXiv e-prints*
- Ji S., Oh S. P., Masterson P., 2019, *MNRAS*, 487, 737
- Kereš D., Katz N., Weinberg D. H., Davé R., 2005, *MNRAS*, 363, 2
- Kimm T., Devriendt J., Slyz A., Pichon C., Kassin S. A., Dubois Y., 2011, *ArXiv e-prints*
- Konstandin L., Girichidis P., Federrath C., Klessen R. S., 2012, *ApJ*, 761, 149
- Leclercq F. et al., 2017, *A&A*, 608, A8
- Li Y., Bryan G. L., Quataert E., 2019, *ApJ*, 887, 41
- Li Z., Hopkins P. F., Squire J., Hummels C., 2019, *arXiv e-prints*, *arXiv:1909.02632*
- Mandelker N., den van Bosch F. C., Nagai D., Dekel A., Birnboim Y., Aung H., 2020, *arXiv e-prints*, *arXiv:2003.01724*
- Mandelker N., Nagai D., Aung H., Dekel A., Padnos D., Birnboim Y., 2019a, *MNRAS*, 484, 1100
- Mandelker N., Padnos D., Dekel A., Birnboim Y., Burkert A., Krumholz M. R., Steinberg E., 2016, *MNRAS*, 463, 3921
- Mandelker N., van den Bosch F. C., Springel V., van de Voort F., 2019b, *ApJ*, 881, L20
- Mandelker N., van Dokkum P. G., Brodie J. P., van den Bosch F. C., Ceverino D., 2018, *ApJ*, 861, 148
- Martin D. C., Chang D., Matuszewski M., Morrissey P., Rahman S., Moore A., Steidel C. C., 2014a, *ApJ*, 786, 106
- Martin D. C., Chang D., Matuszewski M., Morrissey P., Rahman S., Moore A., Steidel C. C., Matsuda Y., 2014b, *ApJ*, 786, 107
- Martin D. C. et al., 2019, *Nature Astronomy*, 372
- Massaglia S., Rossi P., Bodo G., Ferrari A., 1996, *Astrophysical Letters and Communications*, 34, 295
- Massaglia S., Trussoni E., Bodo G., Rossi P., Ferrari A., 1992, *A&A*, 260, 243
- Matsuda Y., Yamada T., Hayashino T., Yamauchi R., Nakamura Y., 2006, *ApJ*, 640, L123
- Matsuda Y. et al., 2011, *MNRAS*, 410, L13
- McCourt M., Oh S. P., O’Leary R., Madigan A.-M., 2018, *MNRAS*, 473, 5407
- Micono M., Bodo G., Massaglia S., Rossi P., Ferrari A., Rosner R., 2000, *A&A*, 360, 795
- Nelson D., Genel S., Pillepich A., Vogelsberger M., Springel V., Hernquist L., 2016, *MNRAS*, 460, 2881
- Nelson D., Vogelsberger M., Genel S., Sijacki D., Kereš D., Springel V., Hernquist L., 2013, *MNRAS*, 429, 3353
- Ocvirk P., Pichon C., Teyssier R., 2008, *MNRAS*, 390, 1326
- Ostriker J., 1964, *ApJ*, 140, 1056
- Padnos D., Mandelker N., Birnboim Y., Dekel A., Krumholz M. R., Steinberg E., 2018, *ArXiv e-prints*
- Padoan P., Nordlund A., Jones B. J. T., 1997, *MNRAS*, 288, 145
- Peeples M. S. et al., 2019, *ApJ*, 873, 129
- Pichon C., Pogosyan D., Kimm T., Slyz A., Devriendt J., Dubois Y., 2011, *MNRAS*, 418, 2493
- Price D. J., Federrath C., Brunt C. M., 2011, *ApJ*, 727, L21
- Prochaska J. X., Lau M. W., Hennawi J. F., 2014, *ApJ*, 796, 140
- Rees M. J., Ostriker J. P., 1977, *MNRAS*, 179, 541
- Roca-Fàbrega S. et al., 2019, *MNRAS*, 484, 3625
- Rossi P., Bodo G., Massaglia S., Ferrari A., 1997, *A&A*, 321, 672
- Scalo J., Vázquez-Semadeni E., Chappell D., Passot T., 1998, *ApJ*, 504, 835
- Scannapieco E., Brüggemann M., 2015, *ApJ*, 805, 158
- Schneider E. E., Robertson B. E., 2017, *ApJ*, 834, 144
- Shapiro K. L. et al., 2008, *ApJ*, 682, 231
- Simons R. C. et al., 2019, *ApJ*, 874, 59
- Springel V., 2010, *MNRAS*, 401, 791
- Stark D. P., Swinbank A. M., Ellis R. S., Dye S., Smail I. R., Richard J., 2008, *Nature*, 455, 775
- Steidel C. C., Adelberger K. L., Shapley A. E., Pettini M., Dickinson M., Giavalisco M., 2000, *ApJ*, 532, 170
- Stewart K. R., Brooks A. M., Bullock J. S., Maller A. H., Diemand J., Wadsley J., Moustakas L. A., 2013, *ApJ*, 769, 74
- Stewart K. R., Kaufmann T., Bullock J. S., Barton E. J., Maller A. H., Diemand J., Wadsley J., 2011, *ApJ*, 738, 39
- Stone J. M., Xu J., Hardee P., 1997, *ApJ*, 483, 136

- Suresh J., Nelson D., Genel S., Rubin K. H. R., Hernquist L., 2019, MNRAS, 483, 4040  
 Teyssier R., 2002, A&A, 385, 337  
 Toro E. F., Spruce M., Speares W., 1994, Shock Waves, 4, 25  
 van de Voort F., Schaye J., 2012, MNRAS, 423, 2991  
 van de Voort F., Schaye J., Altay G., Theuns T., 2012, MNRAS, 421, 2809  
 van de Voort F., Schaye J., Booth C. M., Haas M. R., Dalla Vecchia C., 2011, MNRAS, 414, 2458  
 van de Voort F., Springel V., Mandelker N., van den Bosch F. C., Pakmor R., 2019, MNRAS, 482, L85  
 van Leer B., 1977, Journal of Computational Physics, 23, 263  
 Vazquez-Semadeni E., 1994, ApJ, 423, 681  
 Vietri M., Ferrara A., Miniati F., 1997, ApJ, 483, 262  
 Vogelsberger M., Sijacki D., Kereš D., Springel V., Hernquist L., 2012, MNRAS, 425, 3024  
 Vossberg A.-C., Cantalupo S., Pezzulli G., 2019, arXiv e-prints, arXiv:1904.05350  
 Wechsler R. H., Tinker J. L., 2018, ARA&A, 56, 435  
 White S. D. M., Rees M. J., 1978, MNRAS, 183, 341  
 Wisnioski E. et al., 2015, ApJ, 799, 209  
 Xu J., Hardee P. E., Stone J. M., 2000, ApJ, 543, 161

## APPENDIX A: CONVERGENCE TESTS

We repeated three of our simulations, M1.0\_d100, M2.0\_d100, and M1.0\_d100\_HD, with several different resolutions, ranging from 128 cells across the stream diameter (our fiducial resolution) to 16 cells across the stream diameter. We present the results of this study in Fig. A1. In the left-hand panel we show the cold mass as a function of time, similar to the left-hand panel of Fig. 5. In the centre and right-hand panels we show the net energy dissipation rate and the net cooling rate in our simulations, similar to the left-hand and centre panels of Fig. 13. Note that since the energy dissipation is governed by the mass entrainment, convergence in the left-hand panel implies convergence in the centre and right-hand panels, but we show all three for completeness. Our results are approximately converged even at very low resolutions, with only 16 cells across the stream diameter. For the M1.0\_d100 and M2.0\_d100 cases, There is a slight tendency for the entrainment rate and the energy dissipation rate to be higher in lower resolution simulations, but this is a small effect. G20 reported similar convergence properties of the mass entrainment rate in their cloud crushing simulations with radiative cooling.

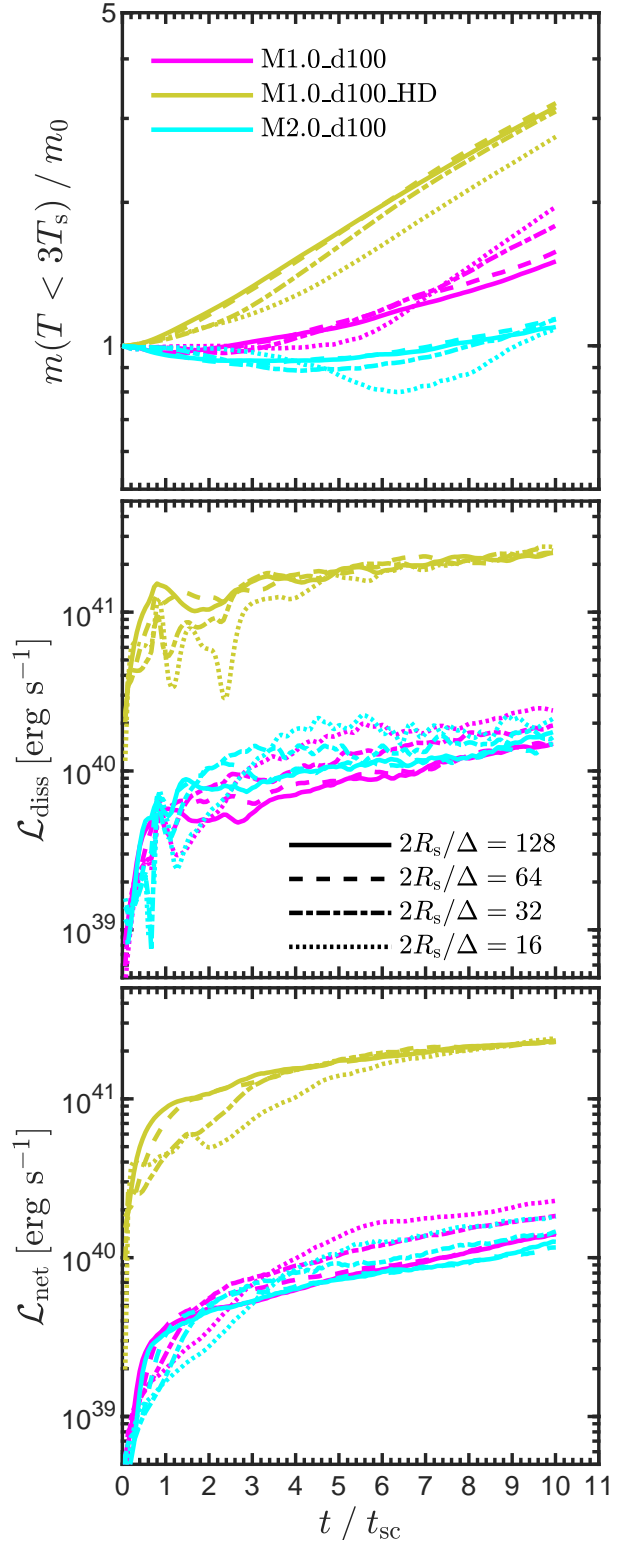


**Figure A1.** Convergence tests. We show as a function of time normalized by the stream sound crossing time, the mass of cold gas normalized by the initial stream mass (*left*, similar to Fig. 5 left), the net energy dissipation rate (*centre*, similar to Fig. 13 left), and the net cooling rate (*right*, similar to Fig. 13 centre). Different colours represent different simulations as in Figs. 5-13, while different line styles represent different resolutions, as indicated in the legend. Our results appear converged even at very low resolution of 16 cells across the stream diameter.